공학석사 학위논문

직관내 기포의 흐름에 대한 2 차원 수치 모의

2D Numerical Simulations of Bubble Flow in Straight Pipes

2016 년 8 월

서울대학교 대학원

건설환경공학부

이 태 윤

ABSTRACT

The main purpose of water aeration is to maintain healthy levels of dissolved oxygen (DO) concentration. Water aeration involves the injection of air or air bubbles into water treatment reservoir commonly through pipes. Fine bubble has higher mass transfer when its diameter gets smaller and smaller bubbles are more capable of enhancing DO concentration level. Two-phase flow consisting of air and water inside horizontal pipe with small diameter is capable of transferring fine bubbles into a body of water and its mechanism should be clearly understood for better system designing. Nevertheless, there are only a few studies that deal with the relationship between mathematical characteristics of two-phase flow inside horizontal pipe and DO concentration level. The main objective of this study is to perform 2-dimensional two-phase simulations inside horizontal pipe using the computational fluid dynamics (CFD) OpenFOAM (Open source Field Operation And Manipulation) tools to examine the effect of pipe wall shear stress on bubble size, which is the major factor effecting DO concentration level. Under different initial conditions, two-phase numerical simulations using Reynolds-averaged Navier-Stokes (RANS) combined with Eulerian-Eulerian method were performed to compute the axial Sauter Mean Diameter (SMD) of bubbles, water velocity, and wall shear stress within a 13.4 m long horizontal pipe with 50.3 mm inner diameter. The coalescence and breakage of bubbles caused by random collisions were considered during the simulations to predict the values of axial SMD. The water velocity and SMD were validated against the experimental data of Kocamustafaogullari and Wang (1991) and the relative errors ranged from 4% to 15% and 8% to 30%, respectively. Two additional experimental results obtained by Yin et al. (2012) and Water Supply Engineering Laboratory (WSEL) at SNU were gathered. These experiments deal with two-phase horizontal pipe flow under different configurations and DO concentration level. Their results were compared with the results obtained by Kocamustafaogullari and Wang (1991) and the aforementioned numerical analysis to determine the effect of pipe wall

shear stress on bubble diameter and DO concentration level. As a result, the increase in pipe wall shear stress decreases bubble size and increases DO concentration level. By comparing the results and making links between them, it was concluded that the pipe wall shear stress plays a key role in breaking up the bubbles.

Keywords: OpenFOAM, 2D CFD Modeling, Two-Phase Pipe Flow, Bubble Coalescence and Breakup, Sauter Mean Diameter, DO Concentration.
Student Number: 2014-22711

TABLE OF CONTENTS

LIST OF FIGURES

LIST OF TABLES

CHAPTER 1. INTRODUCTION

1.1 General Introduction

The main purpose of water aeration is to maintain healthy levels of dissolved oxygen (DO) concentration, which is the most important water quality factor. Water aeration involves the injection of air or air bubbles into water treatment reservoir commonly through pipes. Fine bubbles have a higher mass transfer when the diameter of the bubble gets smaller (Kim, 2010) and smaller bubbles are more capable of enhancing DO concentration level (Yin et al., 2012). Two-phase flow consisting of air-water inside horizontal pipe with small diameter is capable of transferring fine bubbles into a body of water and its mechanism should be clearly understood for better system designing. Nevertheless, there are only a few studies that deal with the relationship between mathematical characteristics of two-phase flow inside horizontal pipe and DO concentration level. The hydrodynamics in bubbly flows in horizontal pipe can be determined by the bubble size distribution, gas and liquid velocity, and gas volume fraction. In the flow, the size of the bubble can undergo continuous change due to breakup and coalescence. Accurate description and investigation of bubble size and its distribution in two phase flow are therefore of paramount importance in correctly simulating two-phase flow behavior. The local spatial and geometrical internal structure including bubble diameter or interfacial area concentration in such flow were found to be affected by the coalescence and break-up through the interactions among bubbles as well as between bubbles and turbulent eddies in turbulent flows.

1.2 Objective and Necessities

Pipes' operating conditions are important for controlling the efficiency and effectiveness of aeration process. Even though many studies have been conducted on two-phase flows in pipes, there are a few studies to deal with millimeter scale bubble flow inside straight horizontal pipes. The main objective of this study is to perform 2-dimensional two-phase simulations inside horizontal pipe using the computational fluid dynamics (CFD) OpenFOAM (Open source Field Operation And Manipulation) tools to examine the effect of pipe wall shear stress on bubble size, which is the major factor effecting DO concentration level. Under different initial conditions, two-phase numerical simulations using Reynolds-averaged Navier-Stokes (RANS) combined with Eulerian-Eulerian method were performed to compute the axial Sauter Mean Diameter (SMD) of bubbles, water velocity, and wall shear stress within a 13.4 m long horizontal pipe with 50.3 mm inner diameter. The coalescence and breakage of bubbles caused by random collisions were considered during the simulations to predict the values of axial SMD. The SMD and water velocity values were validated against the experimental data of Kocamustafaogullari and Wang (1991).

Two additional experimental results obtained by Yin et al. (2012) and Water Supply Engineering Laboratory (WSEL) at SNU were gathered. These experiments deal with two-phase horizontal pipe flow under different configurations and DO concentration level. Their results were compared with the results obtained by Kocamustafaogullari and Wang (1991) and the aforementioned numerical analysis to determine the effect of pipe wall shear stress on bubble diameter and DO concentration level.

CHAPTER 2. THEORETICAL BACKGROUND

2.1 Previous Studies

2.1.1 Two-Phase Flow

In the past decades, significant developments in air and water two-phase flow modeling have arisen since the introduction of the two-phase model. In order to examine and analyze the flow patterns and bubble formation during two-phase bubbly flow under various pipe configurations, significant attention has been paid towards understanding the coalescence and breakage of bubbles caused by interactions among them. Several experimental studies have been performed to describe the flow patterns in horizontal bubbly flow.

Govier and Aziz (1972) have classified the flow patterns into five groups and they are bubbly, plug, slug, wave and annular. Taitel and Dukler (1976) have mapped these flow regimes in a two-dimensional coordinate system and predicted their transition for numerous fluid properties and pipe sizes. Kocamustafaogullari and Wang (1991), Kocamustafaogullari and Huang (1994), Kocamustafaogullari et al. (1994), Andreussi et al. (1999), Iskandrani and Kojasoy (2001), Razzaque et al. (2003), Sanders et al. (2004) and Yang et al. (2004). Haoues et al. (2009) and Talley and Kim (2010) have developed a two-phase model to predict the flow characteristics of horizontal bubbly flow.

2.1.2 Bubble Coalescence and Breakup

In order to study the bubble size distribution and its flow patterns, the population balance approach has been used to accommodate the complex bubble interaction mechanisms coupled with the air and water two-fluid model.

Ekambara et al. (2008) have applied the MUSIG model while Li et al. (2010) have adopted the Average Bubble Number Density (ABND) approach in order to investigate the internal phase distribution of a horizontal bubbly flow. For air and water and two phase turbulence interactions, the major mechanisms have been identified by Prince and

Blanch (1990): coalescence due to random collision driven by turbulent eddies, coalescence caused by the acceleration of the following bubble in the wake of the preceding bubble, and break-up occurred due to the impact of turbulent eddies.

2.1.3 Bubble Diameter and DO Concentration Level

The relationship between bubble diameter and dissolved oxygen concentration has been studied over many years. Camp (1963) has argued that gas transfer is achieved mainly through small air bubbles and their sizes determine the transfer rate.

Cumby (1987) has mentioned that smaller the gas bubble, the larger interfacial area per unit volume and due to this reason, bubbles of smaller size are better for enhancing oxygen transfer.

DeMoyer et al. (2003) performed several experiments and from their experiments, they have concluded that the total oxygen transfer takes place through the bubble-water interface. They obtained the results numerically and verified them experimentally.

Fayolle et al. (2007) performed numerical studies and they have shown that when the bubble size decreases by 10%, the oxygen transfer coefficient increases by 15%. When the bubble diameter increases by 10% the oxygen transfer coefficient decreases by 11%.

Kim (2010) has argued that fine bubbles have a higher mass transfer when the diameter of the bubble gets smaller and Yin et al. has argued that smaller bubbles are more capable of enhancing DO concentration level.

2.1.4 Two-Phase Flow Pipe Wall Shear Stress

Shear stress mechanisms involved in air and water two-phase flow are very difficult to predict and analyze. In order to study shear stress in two-phase, one should rely on several assumptions and empirical equations.

Taitel and Dukler (1976) have presented a shear stress model which involves momentum balance of the gas and liquid phases. Andritsos and Hanratty (1987) has argued that wall shear stress induced by liquid is better predicted through characteristic stress τ_c.

Various techniques have been used to measure wall shear stress. Cravarolo et al. (1964) and Kirillov et al. (1978) have reported the method for direct measurements of average wall shear stress. Cognet et al. (1984) have used indirect methods based on the analogy between momentum transfer and mass transfer and Whalley and McQuillan (1985) have used indirect methods based on heat transfer.

Kowalski (1987) has used hot film probes to measure the wall shear stress for circular pipe at various radial locations in the gas region. From the experiment, it was concluded that the models used for estimation of the gas wall shear stress seem to be appropriate.

CHAPTER 3. METHODOLOGIES

3.1 RANS Governing Equations

3.1.1 RANS Combined with Eulerian-Eulerian

The Reynolds-Averaged Navier–Stokes (RANS) equations are time-averaged equations of motion for fluid flow. Each variable is decomposed into its time-averaged and fluctuating quantities and RANS equations are primarily used to describe behaviors of turbulent flows.

Applying Reynolds time-averaging to the incompressible form of the Navier-Stokes equations leads to the RANS equations describing the time variation of mean flow quantities. The RANS describing the time-evolution of the mean flow quantities U_i and P can be written as:

$$\frac{\partial U_i}{\partial x_i} = 0 \tag{3.1.1.1}$$

$$\frac{\partial U_i}{\partial t} + U_i \frac{\partial U_i}{\partial x_i} + \frac{1}{\rho}\frac{\partial P}{\partial x_i} = \frac{1}{\rho}\frac{\partial}{\partial x_i}(\bar{\tau}_{ij} + \lambda_{ij}) \tag{3.1.1.2}$$

To simulate bubbly flows, the Eulerian-Eulerian model (Becker, Sololichin and Eigenberger, 1994) combined with RANS was employed. Based on the Eulerian-Eulerian two-fluid model, the Reynolds -averaged continuity and momentum equations for phase c are written as (Yang, 2014):

$$\frac{\partial(\rho_c \alpha_c)}{\partial t} + \frac{\partial(\rho_c \alpha_c u_{cj} + \rho_c \overline{\alpha_c' u_{cJ}'})}{\partial x_j} = 0 \tag{3.1.1.2}$$

$$\frac{\partial(\rho_c \alpha_c u_{ci})}{\partial t} + \frac{\partial(\rho_c \alpha_c u_{ci} u_{cj})}{\partial x_j} = -\alpha_c \frac{\partial P}{\partial x_i} + \frac{\partial(\alpha_c \overline{\tau_{cIJ}})}{\partial x_j} + F_{ci} + \rho_c \alpha_c g_i$$
$$-\rho_c \frac{\partial}{\partial x_j}(\alpha_c \overline{u_{cI}' u_{cJ}'} + u_{ci}\overline{\alpha_c' u_{cJ}'} + u_{cj}\overline{\alpha_c' u_{cI}'} + \overline{\alpha_c' u_{cI}' u_{cJ}'}) \tag{3.1.1.4}$$

$$\sum \alpha_c = 1 \tag{3.1.1.5}$$

Where α_c is the phase volume fraction.

The correlation term of phase holdup and velocity fluctuations $\overline{\alpha_c' u_{cl}'}$ in both continuity and momentum equations represent the transport of both mass and momentum by dispersion. Since the influence of the dispersed phase on turbulence structure is not well understood, a simple gradient assumption can be adopted to model $\overline{\alpha_c' u_{cl}'}$, which is giver by (Yang, 2014):

$$\overline{\alpha_c' u_{cl}'} = -\frac{\upsilon_{ct}}{\sigma_t}\frac{\partial \alpha_c}{\partial x_i} \tag{3.1.1.6}$$

where is σ_t is the Schmidt number for the phase dispersion. The value of this number depends on the size of the dispersed phase and the scale of turbulence. It was found that the simulation results were sensitive to σ_t in gas-liquid systems and the value of 1.0 was recommended (Ranade and Van den Akker, 1994), but Wang and Mao (2002) suggested a value of 1.6 was suitable (Yang, 2014).

3.2 Turbulence Model: k-ε Model

3.2.1 Dispersed k-ε Model

When the RANS method is employed, the velocity fluctuation correlation term $\overline{u_{cl}' u_{cJ}'}$, namely the Reynold stress, will appear. For the closure of momentum equations, this term should be treated by involving known or calculable quantities. This can be done through k-ε turbulence model. The Reynolds stresses are treated based on the Boussinesq gradient hypothesis:

$$\overline{u'_{ci}u'_{cJ}} = \frac{2}{3}k\delta_{ij} - \nu_{ct}\left(\frac{\partial u_{cj}}{\partial x_i} + \frac{\partial u_{ci}}{\partial x_j}\right) \quad (3.2.1)$$

The dispersed phase can affect the turbulence of the system via interphase momentum exchange. The k and ε equations can be written in a general form as:

$$\frac{\partial(\rho_c\alpha_c k)}{\partial t} + \frac{\partial(\rho_c\alpha_c u_{ci}k)}{\partial x_i} = \frac{\partial}{\partial x_i}\left[\alpha_c\frac{\mu_{ct}}{\sigma_k}\frac{\partial k}{\partial x_i}\right] + \frac{\partial}{\partial x_i}\left[k\frac{\mu_{ct}}{\sigma_k}\frac{\partial \alpha_c}{\partial x_i}\right] + S_k \quad (3.2.2)$$

$$\frac{\partial(\rho_c\alpha_c \varepsilon)}{\partial t} + \frac{\partial(\rho_c\alpha_c u_{ci}\varepsilon)}{\partial x_i} = \frac{\partial}{\partial x_i}\left[\alpha_c\frac{\mu_{ct}}{\sigma_\varepsilon}\frac{\partial \varepsilon}{\partial x_i}\right] + \frac{\partial}{\partial x_i}\left[\varepsilon\frac{\mu_{ct}}{\sigma_\varepsilon}\frac{\partial \alpha_c}{\partial x_i}\right] + S_\varepsilon \quad (3.2.3)$$

where $\sigma_k = 1.3$ and $\sigma_\varepsilon = 1.0$. The source terms in the above equations are:

$$S_k = \alpha_c[(G + G_e) - \rho_c\varepsilon] \quad (3.2.4)$$

$$S_\varepsilon = \frac{\alpha_c\varepsilon}{k}[C_1(G + G_e) - C_2\rho_c\varepsilon] \quad (3.2.5)$$

where G is the turbulent generation and G_e is the extra production term due to the dispersion phase. Based on the analysis of Kataoka et al. (1992), G_e is mainly dependent on the grad force between the continuous phase and the dispersed phase:

$$G = -\rho_c\alpha_c\overline{u'_{ci}u'_{cJ}}\frac{\partial u_{ci}}{\partial x_j} \quad (3.2.6)$$

$$G_e = \sum_d C_b|F|\left(\sum(u_{di} - u_{ci})^2\right)^{0.5} \quad (3.2.7)$$

where C_b is an empirical coefficient. When $C_b = 0$, the energy induced by the dispersed phase dissipates at the interface and has no influence on the turbulent kinetic energy of the continuous phase. According to the analysis in the literature, the value of C_b has always been set as 0.02. The component of rate of deformation, the eddy viscosity if defined as:

$$\nu_{ct} = \frac{\rho_c C_\mu k^2}{\varepsilon} \quad (3.2.8)$$

And other model constants are $C_\mu = 0.09,\ C_1 = 1.44,\ C_2 = 1.92.$

3.3 Bubble Coalescence

3.3.1 Mechanisms of Bubble Coalescence

As shown in Figure 3.3.1.1, coalescence of two bubbles in turbulent flows occurs in three steps:

a) Bubbles collide, trapping a small amount of liquid between them.

b) This liquid then drains until the liquid film separating the bubbles reaches a critical thickness.

c) Film rupture occurs

b) Coalescence occurs.

From the first step, the coalescence rate is intimately connected to the collision rate. In order to determine whether a given collision will result in coalescence, it is necessary to determine the collision efficiency. Two bubbles will coalesce provided they remain in contact for a period of time sufficient for the liquid film between them to thin to the critical value necessary for rupture (Prince, 1990). Collisions occur due to a variety of mechanisms such as turbulence, buoyancy and laminar shear. It is clear that collisions may result from the random motion of bubbles due to turbulence. In addition, bubbles of different sizes will have different rise velocities which may lead to collision (Prince, 1990).

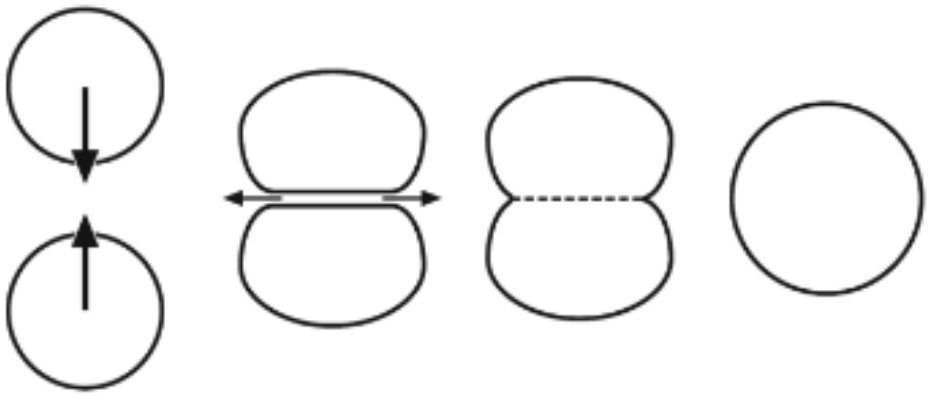

Figure 3.3.1.1: Coalescence of two bubbles in turbulent flows occurs in four steps (Jakobsen, 2014).

3.3.2 Turbulent Collision rate

Following Kennard (1938), the collision frequency resulting from turbulent motion (θ_{ij}^{T}) can be expressed as a function of bubble size, concentration and velocity:

$$\theta_{ij}^{T} = n_i n_j S_{ij} \left(\bar{u}_{ti}^2 + \bar{u}_{tj}^2\right)^{1/2} \tag{3.3.2.1}$$

where n_i and n_j are the concentrations of bubble of radius r_{bi} and r_{bj}, respectively, $\bar{u}_t$ is the average turbulent fluctuating velocity of the bubble and S_{ij} is the collision cross-sectional area of the bubbles defined by:

$$S_{ij} = \frac{\pi}{4}\left(r_{bi} + r_{bj}\right)^2 \tag{3.3.2.2}$$

The velocity of bubbles in Eq. 3.3.2.1 is assumed to be the turbulent eddy velocity of the length scale of the bubble. Eddy motion of this scale is primarily responsible for the relative motion between bubbles. Very small eddies do not contain sufficient energy to significantly influence bubble motion, while eddies much larger than the bubble size transport groups of bubbles without leading to significant relative motion (Prince, 1990).

In determining a value for the turbulent velocity of a bubble requires restrictive assumptions regarding the mechanisms of turbulence. Generally, it is very common to assume that the turbulence is isotropic and the sizes of bubble lie in the inertial subrange. These two assumptions are required in order to make the problem tractable.

The second assumption in determining the turbulent velocity of the bubble is that the bubble size lies in the inertial subrange. This criteria is typically examined in terms of the inverse radius or wave number. The criteria for the inertial subrange is that (Prince 1990):

$$k_e \ll k_b \ll k_d$$

where k_e, is the wave number of the large energy containing eddies, k_b, is the wave number corresponding to the bubble size and k_d, is the wave number of the eddies of viscous dissipation. The wave number for energy dissipation, equivalent to the inverse of the microscale of turbulence, is defined by Batchelor (1953) as:

$$k_d = 0.5\frac{\varepsilon^{1/4}}{\nu^{3/4}} \tag{3.3.2.3}$$

3.3.3 Collision Efficiency

It is necessary to estimate the collision efficiency in order to determine what fraction of binary bubble collisions lead to coalescence. This efficiency is a function of the contact time between two bubbles and the time required for them to coalesce. An expression for the efficiency (λ_{ij}) is given by Coulaloglou and Tavlarides (1977):

$$\lambda_{ij} = exp(-\frac{t_{ij}}{\tau_{ij}}) \tag{3.3.3.1}$$

where t_{ij} is the time required for coalescence of bubbles of radius r_{bi} and r_{bj} defined by:

$$t_{ij} = \left\{\frac{r_{ij}^3\rho_l}{16\sigma}\right\}^{\frac{1}{2}} ln\frac{h_0}{h_f} \tag{3.3.3.2}$$

where h_0 is the initial film thickness, h_f is the critical film thickness where rupture occurs, and r_{ij} is the equivalent radius, which is given by Chester and Hoffman (1982) as:

$$r_{ij} = \frac{1}{2}\left(\frac{1}{r_{bi}} + \frac{1}{r_{bj}}\right)^{-1} \tag{3.3.3.3}$$

In Eq. (3.3.3.1), τ_{ij} is the contact time for the two bubbles and it is given by:

$$\tau_{ij} = \frac{r_b^{2/3}}{\varepsilon^{1/3}} \tag{3.3.3.4}$$

The coalescence rate of bubbles of radii r_{bi} and r_{bi} (Γ_{ij}) is given by the total collision frequency multiplied by the efficiency (Prince, 1990):

$$\Gamma_{ij} = \left(\theta_{ij}^T\right) \times \exp\left(-\frac{t_{ij}}{\tau_{ij}}\right) \tag{3.3.3.5}$$

From the equation above, an expression for the overall coalescence rate can be obtained and it is the following (Prince, 1990):

$$\Gamma_T = \frac{1}{2}\sum_i \sum_j (\theta_{ij}^T) \times \exp(-\frac{t_{ij}}{\tau_{ij}}) \tag{3.3.3.6}$$

The factor $\frac{1}{2}$ is included to avoid counting coalescence events between bubble pairs twice.

3.4 Bubble Breakup

3.4.1 Mechanisms of Bubble Breakup

Many studies on bubble break-up is mostly derived from Hinze (1955). Bubble break-up occurs mainly through the interactions between bubbles and turbulent eddies. The sizes of eddy are responsible for break-up phenomena. Eddies that are equal to or marginally smaller than the bubble size are responsible for break-up of bubbles. Eddies that are larger than bubbles simply transport the bubbles without causing break-up, while eddies smaller than the bubbles do not contain sufficient energy to cause breakage. To obtain an expression for the break-up rate of bubbles, the turbulent collision rate of bubbles with eddies of the appropriate size is considered. According to Kennard (1938), the collision rate is given by:

$$\theta_{ie} = n_i n_e S_{ie} \left(\bar{u}_{ti}^2 + \bar{u}_{te}^2\right)^{\frac{1}{2}} \tag{3.4.1.1}$$

which is analogous to Eq. 3.3.2.1 with the eddy diameter, concentrations, and velocity replacing that of one of the bubbles.

3.4.2 Breakup Efficiency

Not all bubble-eddy collisions are likely to result in bubble break-up. The criterion for break-up relates the energy of the eddy to the surface tension forces of the bubble. The balance of disruptive and cohesive forces is generally expressed in terms of the dimensionless Weber number (Prince, 1990):

$$W_e = \frac{u^2 d_b \rho_l}{\sigma} \tag{3.4.2.1}$$

A critical Weber number will exist at the point where cohesive and disruptive forces balance, resulting in a maximum stable bubble size. Bhavaraju et al. (1978) provide an expression for the maximum stable bubble size in turbulent gas-liquid flows (Prince, 1990):

$$d_m = 1.12 \frac{\sigma^{0.6}}{\left(\frac{\psi}{V_l}\right)^{0.4} \rho^{0.2}} \left(\frac{\mu_c}{\mu_d}\right)^{0.1} \tag{3.4.2.2}$$

d_m, is the maximum stable bubble size, V_l, is the total volume of liquid and μ_c and μ_d are the viscosities of the continuous and dispersed phases, respectively. From this expression and Eq. 3.4.2.1, one may obtain a critical Weber number of 2.3 for air bubbles in water. This is translated into a critical eddy velocity (u_{ci}) for break-up of a bubble of radius, r_{bi}:

$$u_{ci} = 1.52 \left(\frac{\sigma}{r_{bi}}\right)^{1/2} \tag{3.4.2.3}$$

It is necessary to determine which eddies have velocities that exceed this value. To do so, an energy distribution function is required. Angelidou et al. (1979) provide such an expression for a random distribution of energy:

$$X(E_e) = \frac{1}{E_e} exp\left(-\frac{E_e}{\overline{E_e}}\right) \tag{3.4.2.4}$$

Here $X(E_e)$ is the energy distribution function and *E*, is the kinetic energy of the eddy.

Taking the energy of the eddy as proportional to the square of its velocity yields a function of the following form for the fraction of eddies with sufficient energy to cause rupture (Coulaloglou and Tavlarides, 1977):

$$F(u) = exp\left\{-\left(\frac{u_{ci}^2}{u_{te}^2}\right)\right\} \tag{3.4.2.5}$$

where $F(u)$ is the fraction of eddies with sufficient energy to cause rupture and u_{te} is the turbulent velocity of an eddy of radius r_e. This expression is analogous to the collision efficiency for break-up. The break-up rate for a bubble of radius, r_{bi}, is then given by(Prince, 1990):

$$\beta_i = \theta_{ie}\, exp\left(-\frac{u_{ci}^2}{u_{te}^2}\right) \tag{3.4.2.6}$$

and the total break-up rate for all bubbles is (Prince, 1990):

$$\beta_T = \sum_i \sum_e \theta_{ie} \exp\left(-\frac{u_{ci}^2}{u_{te}^2}\right) \tag{3.4.2.7}$$

3.5 Sauter Mean Diameter (d32)

3.5.1 Interfacial Area Transport Equation (IATE) Model

In many multiphase flow contexts, the simplifying assumption that all the disperse phase particles, including bubbles, droplets or solid particles have the same size. However in many natural and technological processes it is necessary to consider the distribution of particle size. One fundamental measure of this is the size distribution function. One measure of the average size that proves useful in characterizing many disperse particulates is the Sauter mean diameter, D32 and this is a measure of the ratio of the particle volume to the particle surface area and, as such, is often used in characterizing particulates (Brennen, 2005).

The Sauter Mean Diameter (d32) values are obtained using a bubble size tracking model called IATE (Interfacial Area Transport Equation) bubble diameter model. It solves for the interfacial curvature per unit volume of the phase rather than interfacial area per unit volume to avoid stability issues relating to the consistency requirements between the phase fraction and interfacial area per unit volume. The transport equations for the particle number, void fraction, and interfacial area concentration can be obtained respectively as Eqs. 3.5.1.1 – 3.5.1.3 (Ishii, 2004):

$$\frac{\partial n}{\partial t} + \nabla \cdot \left(n v_{pm}\right) = \sum_j R_j + R_{ph} \tag{3.5.1.1}$$

$$\alpha(x,t) = \int_{V_{min}}^{V_{max}} f(V,x,t) V dV \tag{3.5.1.2}$$

$$\frac{\partial a_i}{\partial t} + \nabla \cdot (a_i v_i) = \frac{2}{3}\left(\frac{a_i}{\alpha}\right)\left(\frac{\partial \alpha}{\partial t} + \nabla \cdot \alpha v_g - \eta_{ph}\right) + \frac{1}{3\psi}\left(\frac{\alpha}{a_i}\right)^2 \sum_j R_j + \pi D_{bc}^2 R_{ph} \tag{3.5.1.3}$$

where v_{pm}, v_g, v_i, are defined, respectively as:

$$v_{pm}(x,t) = \frac{\int_{V_{min}}^{V_{max}} f(V,x,t) v(V,x,t) dV}{\int_{V_{min}}^{V_{max}} f(V,x,t) dV} \tag{3.5.1.4}$$

$$v_g(x,t) = \frac{\int_{V_{min}}^{V_{max}} f(V,x,t) V v(V,x,t) dV}{\int_{V_{min}}^{V_{max}} f(V,x,t) V dV} \tag{3.5.1.5}$$

$$v_i(x,t) = \frac{\int_{V_{min}}^{V_{max}} f(V,x,t)A_i(V)v(V,x,t)dV}{\int_{V_{min}}^{V_{max}} f(V,x,t)VdV} \quad (3.5.1.6)$$

In Eqs. 3.5.1.4 through 3.5.1.6, R_j and R_{ph} represent the particle source/sink rates per unit mixture volume due to j[th] particle interactions (such as disintegration or coalescence) and that due to phase change, respectively. Hence, the number source/sink rate is defined by:

$$R(x,t) = \int_{V_{min}}^{V_{max}} S(V,x,t)dV \quad (3.5.1.7)$$

In Eqs. 3.5.1.1 – 3.5.1.3, n represents the fluid particle number per unit mixture volume, v_{pm}, the average local particle velocity weighted by the particle number, R_j, the number source/sink rates due to particle interaction, R_{ph}, the number source rate due to the phase change, α, gas void fraction, , the fluid particle volume, a_i, the interfacial area concentration, v_i, fluid particle velocity, v_g, the gas velocity, η_{ph}, the rate of volume generated by nucleation source per unit mixture volume, ψ, the term accounts for the shapes of the fluid particles of interest, and D_{bc}, the critical bubble size.

3.5.2 One-Group a_i Transport Equation

In the one-group formulation, the dispersed bubbles are assumed to be spherical and their interactions are binary. Hence, all the fluid particles of interest are considered to be in the same group in view of their transport mechanisms. Considering that the one-group equation accounts for the bubble transport in the bubbly flow, three interaction mechanisms are identified as the major mechanisms that govern the change in the a_i, such that (Ishii, 2004):

(1) Breakup due to the impact of turbulent eddies (TI)

(2) Coalescence through random collision driven by turbulent eddies (RC)

(3) Coalescence due to the acceleration of the following bubble in the wake of the preceding bubble (WE).

Then, the one-group interfacial area transport equation for air-water bubbly two-phase flow is given by:

$$\frac{\partial a_i}{\partial t} + \nabla \cdot (a_i v_i) = \frac{2}{3}\left(\frac{a_i}{\alpha}\right)\left(\frac{\partial \alpha}{\partial t} + \nabla \cdot \alpha v_g\right) + \frac{1}{3\psi}\left(\frac{\alpha}{a_i}\right)^2 (R_{TI} + R_{RC} - R_{WE}) \quad (3.5.2.1)$$

with

$$R_{TI} = C_{TI}\left(\frac{nu_t}{D_b}\right)\exp\left(-\frac{We_{cr}}{We}\right)\sqrt{1-\frac{We_{cr}}{We}},\ \ where\ We > We_{cr} \quad (3.5.2.2)$$

$$R_{RC} = C_{RC}\left[\frac{n^2 u_t D_b^2}{\alpha_{max}^{1/3}\left(\alpha_{max}^{1/3}-\alpha^{1/3}\right)}\right]\left[1-\exp\left(-C\,\frac{\alpha_{max}^{1/3}\alpha^{1/3}}{\left(\alpha_{max}^{1/3}-\alpha^{1/3}\right)}\right)\right] \quad (3.5.2.3)$$

$$R_{WE} = C_{WE} C_D^{1/3} n^2 D_b^2 u_r \quad (3.5.2.4)$$

3.6 Wall Shear Stress

3.6.1 Circular Pipe Wall Shear Stress

Turbulent flow in a horizontal pipe is considered in this section. The upward eddy motion of fluid particles in a layer of lower velocity to an adjacent layer of higher velocity through a differential area dA as a result of the velocity fluctuation v', as shown in Figure 3.6.1.1.

The mass flow rate of the fluid particles rising through dA is $\rho v' dA$, and its net effect on the layer above dA is a reduction in its average flow velocity because of momentum transfer to the fluid particles with lower average flow velocity. This momentum transfer causes the horizontal velocity of the fluid particles to increase by u', and thus its momentum in the horizontal direction to increase at a rate of $(\rho v' dA)u'$, which must be equal to the decrease in the momentum of the upper fluid layer (Çengel, 2010).

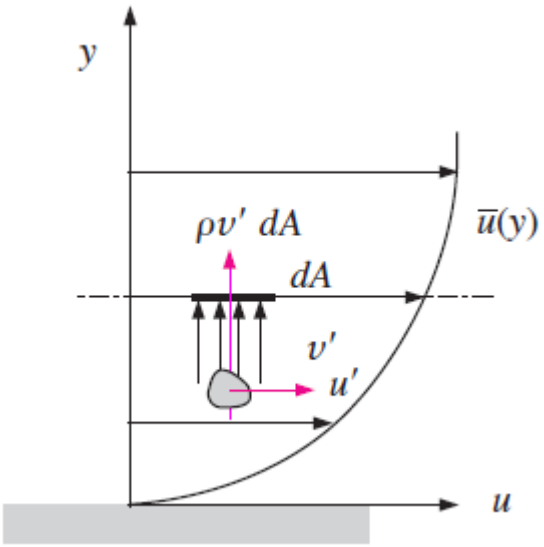

Figure 3.6.1.1: Fluid particle moving upward through a differential area *d*A as a result of the velocity fluctuation (Çengel, 2010).

The horizontal force acting on a fluid element above dA due to the passing of fluid particles through dA is:

$$\delta F = (\rho v' dA)(-u') = -\rho u' v' dA \tag{3.6.1.1}$$

The shear force per unit area due to the eddy motion of fluid particles:

$$\delta F / dA = -\rho u' v' \tag{3.6.1.2}$$

Then the turbulent shear stress can be expressed as:

$$\tau_{turb} = -\rho \overline{u' v'} \tag{3.6.1.3}$$

where $\overline{u'v'}$ is the time average of the product of the fluctuating velocity components u' and v'. Terms such $-\rho u' v'$ is called Reynolds stress or turbulent stress.

The random eddy motion of groups of particles resembles the random motion of molecules in a gas-colliding with each other after traveling a certain distance and exchanging momentum in the process and therefore, momentum transport by eddies in turbulent flows is analogous to the molecular momentum diffusion (Çengel, 2010). In many turbulence models, turbulent shear stress is commonly expressed as:

$$\tau_{turb} = -\rho \overline{u' v'} = \mu_t \frac{\partial \bar{u}}{\partial y} \tag{3.6.1.4}$$

where μ_t is the eddy viscosity or turbulent viscosity, which accounts for momentum transport by turbulent eddies. Then the total shear stress can be expressed as:

$$\tau_{total} = (\mu + \mu_t) \frac{\partial \bar{u}}{\partial y} = \rho(\nu + \nu_t) \frac{\partial \bar{u}}{\partial y} \tag{3.6.1.5}$$

where $\nu_t = \mu_t / \rho$ is the kinematic eddy viscosity or kinematic turbulent viscosity.

The eddy motion loses its intensity close to the wall and diminishes at the wall because of the no-slip condition. The velocity profile is slowly changing in the core region of a turbulent boundary layer, but very steep in the thin layer adjacent to the wall, resulting in large velocity gradients at the wall surface. The velocity gradients at the wall, and thus the wall shear stress, are much larger for turbulent flow than they are for laminar flow, even though the turbulent boundary layer is thicker than the laminar one for the same value of free-stream velocity (Çengel, 2010). So the wall shear stress is much larger in turbulent flow than it is in laminar flow as shown in Figures 6.2.1.2 and 6.2.1.3 (Çengel, 2010).

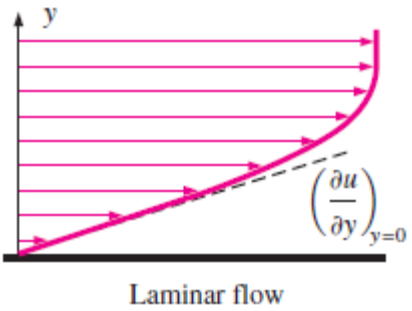

Figure 3.6.1.2: Velocity gradient at the wall for laminar flow (Çengel, 2010).

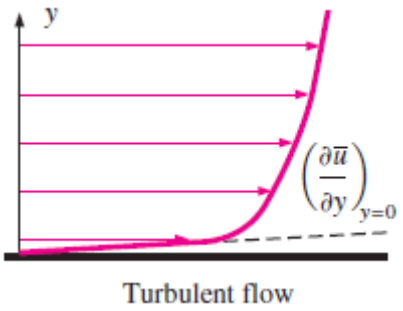

Figure 3.6.1.3: Velocity gradient at the wall for turbulent flow (Çengel, 2010).

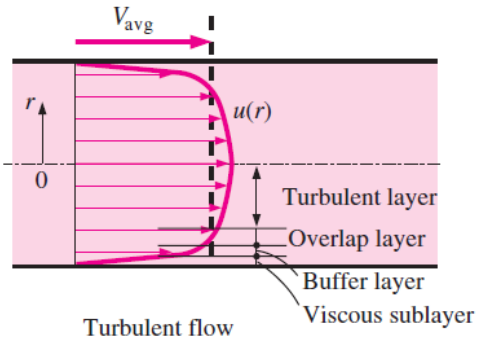

Figure 3.6.1.4: Schematic of layers in turbulent flow (Çengel, 2010).

The velocity gradient in the viscous sublayer remains nearly constant at $\frac{du}{dy} = u/y$, and the wall shear stress can be expressed as:

$$\tau_w = \frac{\mu u}{y} = \frac{\rho \nu u}{y} \quad \text{or} \quad \frac{\tau_w}{\rho} = \frac{\nu u}{y} \tag{3.6.1.6}$$

where y is the distance from the wall. The quantity τ_w/ρ is commonly encountered in turbulent velocity profile analysis. The square root of τ_w/ρ has the dimensions of velocity, and thus it is convenient to view it as a fictitious velocity called the friction velocity expressed as $u_* = \sqrt{\tau_w/\rho}$. Substituting this into Eq. 3.6.1.6, the velocity profile in the viscous sublayer can be expressed in dimensionless form as:

$$\frac{u}{u_*} = \frac{y u_*}{\nu} \tag{3.6.1.7}$$

This equation is known as the law of the wall, and it is found to satisfactorily correlate with experimental data for smooth surfaces for:

$$0 \leq \frac{y u_*}{\nu} \leq 5 \tag{3.6.1.7}$$

The thickness of the viscous sublayer is:

$$y = \delta_{sublayer} = \frac{5\nu}{u_*} = \frac{25}{u_\delta} \tag{3.6.1.8}$$

where u_δ is the flow velocity at the edge of the viscous sublayer. Thus we conclude that the thickness of the viscous sublayer is proportional to the kinematic viscosity and inversely proportional to the average flow velocity. The viscous sublayer is suppressed and it gets thinner as the velocity increases.

The quantity ν/u_* has dimensions of length and is called the viscous length. In boundary layer analysis, it is convenient to work with non-dimensionalized distance and non-dimensionalized velocity defined as:

$$y^+ = \frac{yu_*}{\nu} \quad \text{and} \quad u^+ = \frac{u}{u_*} \tag{3.6.1.9}$$

Eq. 3.6.1.7 becomes:

$$u^+ = y^+ \tag{3.6.1.10}$$

In the overlap layer, the experimental data for velocity are observed to line up on a straight line when plotted against the logarithm of distance from the wall. Dimensional analysis indicates and the experiments confirm that the velocity in the overlap layer is proportional to the logarithm of distance, and the velocity profile can be expressed as (Çengel, 2010):

$$\frac{u}{u_*} = \frac{1}{\kappa} ln \frac{yu_*}{\nu} + B \tag{3.6.1.11}$$

where κ and B are constants and their values are determined experimentally to be about 0.40 and 5.0, respectively. Eq. 3.6.1.11 is the logarithmic law and the velocity profile is determined to be:

$$\frac{u}{u_*} = 2.5\, ln \frac{yu_*}{\nu} + 5.0 \quad or \quad u^+ = 2.5\, ln\, y^+ + 5.0 \tag{3.6.1.11}$$

It turns out that the logarithmic law in Eq. 3.6.1.11 satisfactorily represents experimental data for the entire flow region except for the regions very close to the wall and near the pipe center, as shown in Figure 3.6.1.5, and thus it is viewed as a universal velocity profile for turbulent flow in pipes or over surfaces (Çengel, 2010).

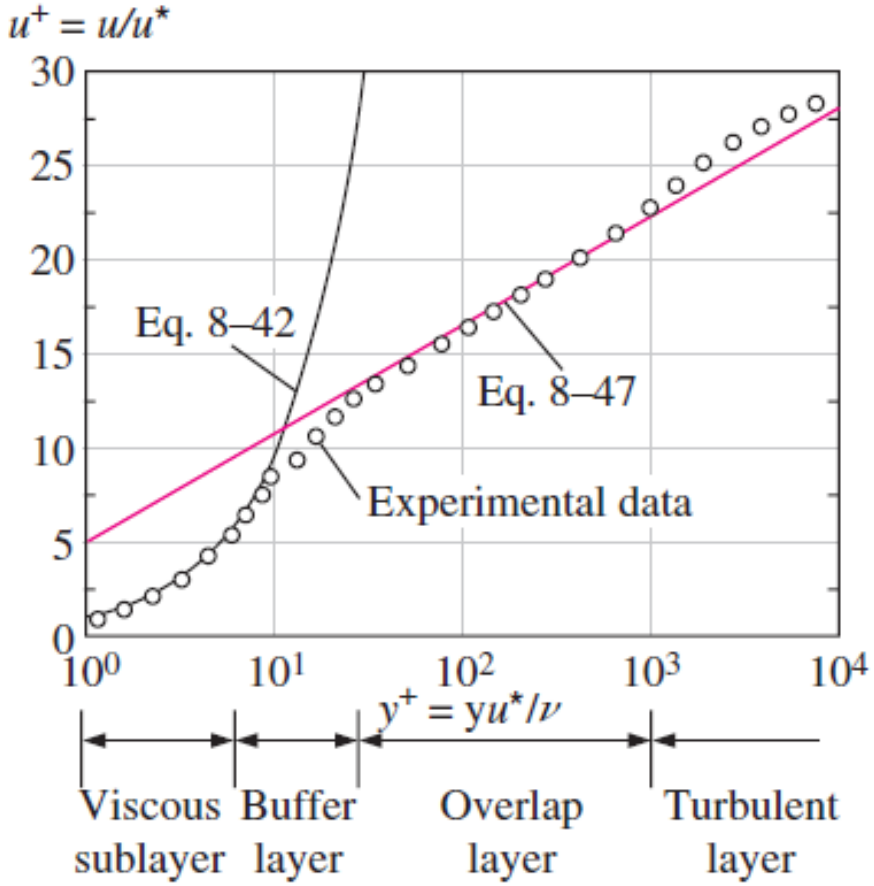

Figure 3.6.1.5: Comparison of the law of the wall and the logarithmic-law velocity profiles with experimental data for fully developed turbulent flow in a pipe (Çengel, 2010).

CHAPTER 4. EXPERIMENTAL SETUP & DATA

4.1 Kocamustafaogullari and Wang (1991)

4.1.1 Experimental Setup & Procedure

Kocamustafaogullari and Wang (1991) designed and built a horizontal flow loop and performed several experiments in order to investigate the interfacial structure of two-phase flow in horizontal pipe. The schematic of the loop is illustrated in Figure 4.1.1.1. The loop consists of various lengths of 50.3 mm diameter circular glass tubes. The entire test section is approximately 15.4 m in length and it is all transparent, so that flow visualization, high-speed photography and high-speed cinematography are possible. More details about the experimental setup can be found in Kocamustafaogullari and Wang (1991).

The experiments were carried out under fully developed bubbly flow conditions by variations in the liquid flow rate, gas flow rate and the radial position of the probe. The superficial liquid velocity was kept constant as 5.1 m/s, and the superficial gas velocities covered a range from 0.25 to 1.37 m/s. Details of the experimental conditions are summarized in Table 4.1.1.1.

Table 4.1.1.1: Experimental conditions, Kocamustafaogullari and Wang (1991)

Case	Pipe Diameter	Pipe Length	Temperature	Inlet Water Velocity	Inlet Air Velocity	Inlet Air Volume Fraction
#	D (m)	L (m)	T (˚C)	j_f (m/s)	j_G (m/s)	(%)
1	0.0503	15.4	25	5.1	0.24	0.043
2				5.09	0.49	0.08
3				4.98	0.8	0.139
4				4.98	1.34	0.204

At fixed liquid superficial velocity, the gas superficial velocity was increased as long as the flow pattern was bubbly. During the operation of the quick-closing valves, the pressure reached sizable proportions of the loop pressure limitations. The temperature of the water was maintained at room temperature by adding tap water to the storage tank. A Vernier, with graduations to an accuracy of 0.0254mm, was used to traverse the probe in a direction perpendicular to the axis of the tube; 23 locations were selected through the pipe diameter of 50.3 mm. The increments were smaller as the probe traversed toward the wall at the upper half of the tube.

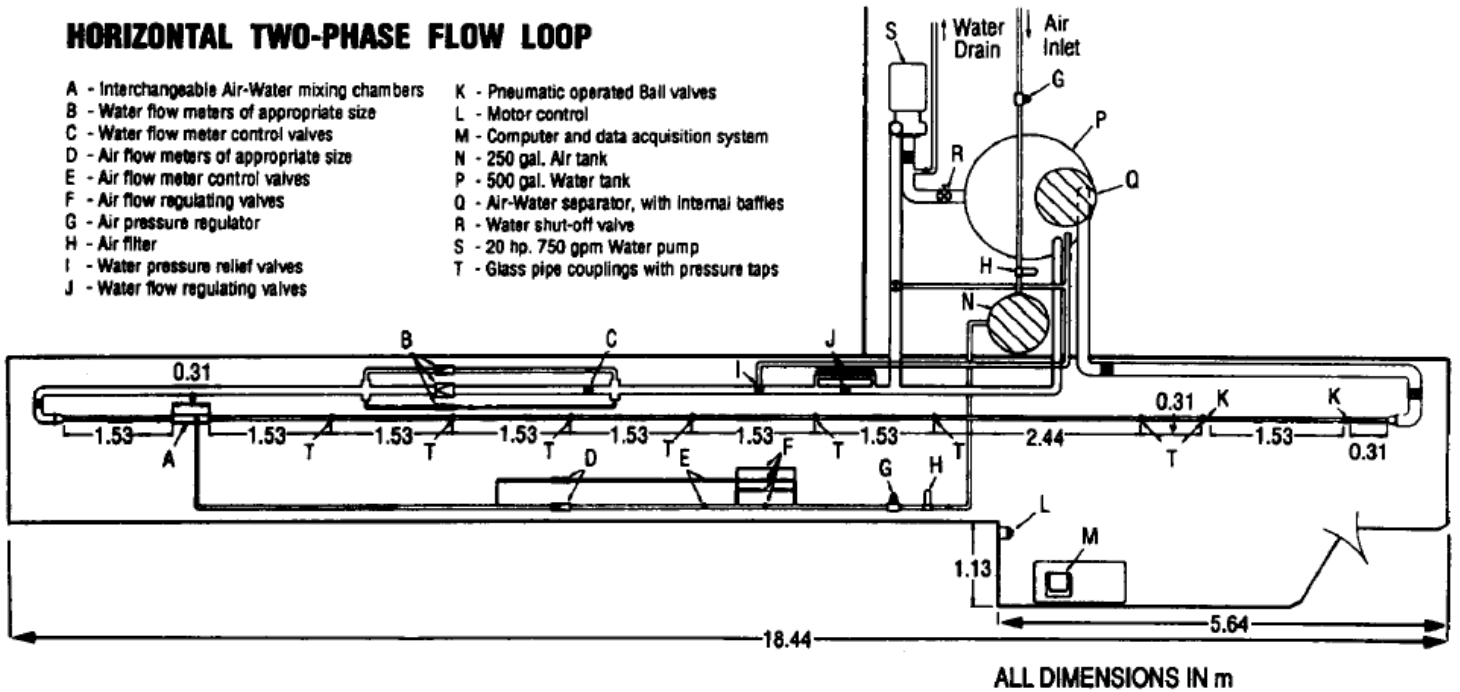

Figure 4.1.1.1: Schematic of the experimental flow loop (Kocamustafaogullari and Wang, 1991).

4.1.2 Experimental Results

The internal phase distribution of co-current, air-water bubbly flow in a 50.3 mm diameter transparent pipeline has been experimentally investigated by using a double-sensor resistivity probe technique. Using the relation between the local interfacial area concentration, void fraction and the Sauter mean diameter of bubbles, the mean bubble diameter distributions were calculated. The Sauter Mean Diameter distributions calculated based on the experiments are illustrated in Figures 4.1.2.1 and 4.1.2.2 at various liquid and gas fluxes. From the figures, it can be observed that the Sauter mean diameters range from about 2 to 5 mm, depending on the location and flow conditions. The profiles show relatively small variations over most of the flow channel cross section except near the wall region. Kocamustafaogullari and Wang (1991) found out that the bubble size tends to reduce close to the wall region and the bubble diameter generally shows an increase with the gas flow rate, although the influence is not significant. Finally, it was noted that the lateral phase distribution for horizontal flow and bubble size distribution are strongly affected by inlet conditions and boundaries. In this study, it was mentioned that future work would include a series of experimental studies to understand how inlet conditions and wall affect the lateral phase distribution for horizontal flow.

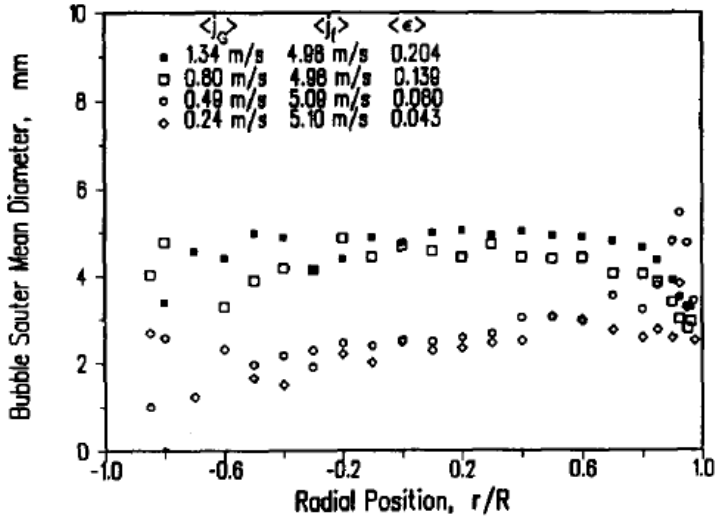

Figure 4.1.2.1: Sauter mean diameter profiles: effect of gas flow loop (Kocamustafaogullari and Wang, 1991).

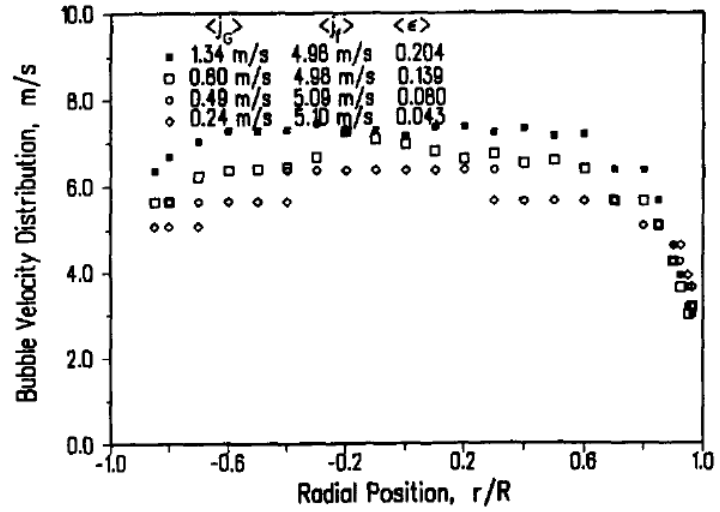

Figure 4.1.2.2: Axial water velocity profiles: effect of gas flow loop (Kocamustafaogullari and Wang, 1991).

4.2 Yin et al. (2012) Numerical Model

4.2.1 Experimental Setup & Procedure

Yin et al. (2012) established a two-phase k-ε mathematical model and a dissolved oxygen transport model using ANSYS FLUENT 12.0 software to investigate whether the mathematical model can be applied to model oxygen transfer by air injection in a horizontal pipe. The developed CFD model was validated against experimental results and a schematic of the experiment's setup is shown in Figure 4.2.1.1.

The experimental setup consists of an 8.81 m long acrylic circular horizontal pipe with inside diameter of 0.13 m and it is connected to two water tanks as shown in Figure 4.2.1.1. Water in the pipe flows from the left water tank to the right tank and is then pumped back to the left tank. The water velocity inside the pipe is measured using a propeller-type velocity meter. Air is injected into the pipe through an aeration hole. The dissolved oxygen level is measured at Section 0-0 and Section 1-1 using two DO probes.

The mathematical model was mainly used to evaluate the effect of pipe's inlet air volume fraction, inlet DO concentration, and travel time of water-air mixture inside the horizontal pipe, on oxygen absorption efficiency, which is an important factor for evaluating DO concentration level in the water body.

Based on the experimental setup and conditions, a total of 125 flow conditions were simulated for an assumed pipe of D = 0.10 m; L = 2 m; and T = 20°C, with the travel time, Δt, (travel time from Section 0-0 to Section 1-1 is defined as $\Delta t = L/U_0$, see Figure 4.2.1.1) increasing from 2.5 to 5, 10, 20, and 40s; C_0 increasing from 0 to 1, 2, 4, and 8 mg/L; and α_0 increasing from 0.005 to 0.01, 0.02, 0.03, and 0.04.

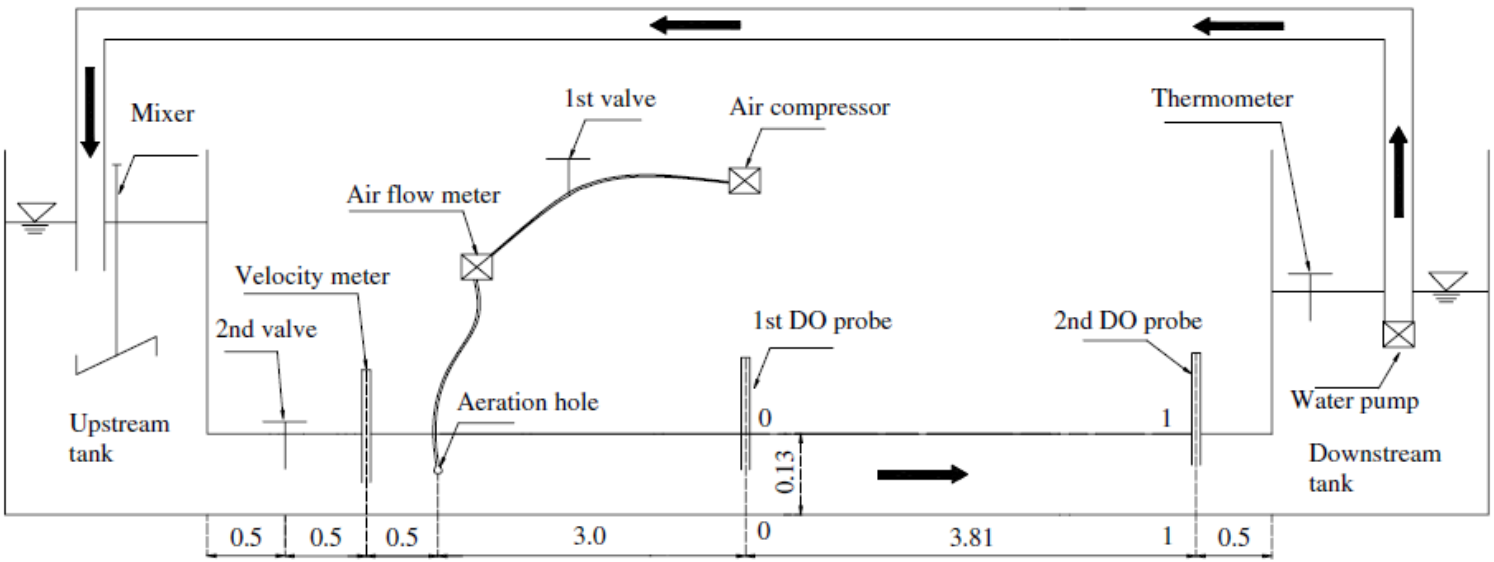

Figure 4.2.1.1: Schematic of the experimental setup (Yin et al., 2012).

4.2.2 Experimental & Numerical Findings

To study the oxygen absorption efficient from the injected air, the oxygen absorption efficiency, F, is defined as follows:

$$F = \frac{C_1 - C_0}{\alpha_0 C_a} \tag{4.2.2.1}$$

where C_a= oxygen concentration of the injected air [in this study C_a= 310 mg/L at the conditions of T=20°C and 101325 Pa (1 atm) pressure]; and α_0= air bubble volume fraction at the inlet boundary. Eq. 4.2.2.1 can be used to estimate the relative absorption amount of oxygen in injected air. Specifically, if *F* = 0, there is no net oxygen transfer from the injected air; thus, $C_1 = C_0$. If *F* = 1, the oxygen in the injected air is transferred completely to the water; thus, $\mathrm{C}_1 = C_0 + \alpha_0 C_a$.

Figure 4.2.2.1 shows the relationship between *F* and C_1/C_s with $\Delta t = 20$ sec. If Δt and α_0 are the same, *F* decreases with the increase of C_0/C_s. The reason is that when C_0/C_s increases, the DO concentration gradient between the water and the bubbles decreases, and the oxygen mass transfer rate decreases, causing the decrease of *F*.

Figure 4.2.2.2 shows the relationship between *F* and α_0 with $C_0/C_s = 0.11$. If C_0/C_s and Δt are the same, *F* decreases with the increase of α_0. Eq. 4.2.2.1 shows that the first derivative of the function *F* with respect to α is a negative number, so *F* decreases with the increase of α_0.

Figure 4.2.2.3 shows the relationship between *F* and Δt for $\alpha_0 = 0.02$. If α_0 and C_0/C_s are the same, *F* increases with the increase of Δt. The reason is that when Δt increases, there is much more time to transfer oxygen from the bubbles to the water, and F increases; however, it increases progressively more slowly owing to the decrease of the oxygen concentration gradient between the water and the bubbles.

Based on the experimental and numerical results, Yin et al. (2012) came to the conclusions that oxygen absorption efficiency decreases with the increase of inlet air volume fraction (Figure 4.2.2.1), but increases with the increase of travel time (Figure

4.2.2.2). However, the mathematical model and its results did not take into account the bubbles' shapes, size distribution, bubble interactions including the collision, coalescence, and breakup, and turbulence characteristics of two-phase flow.

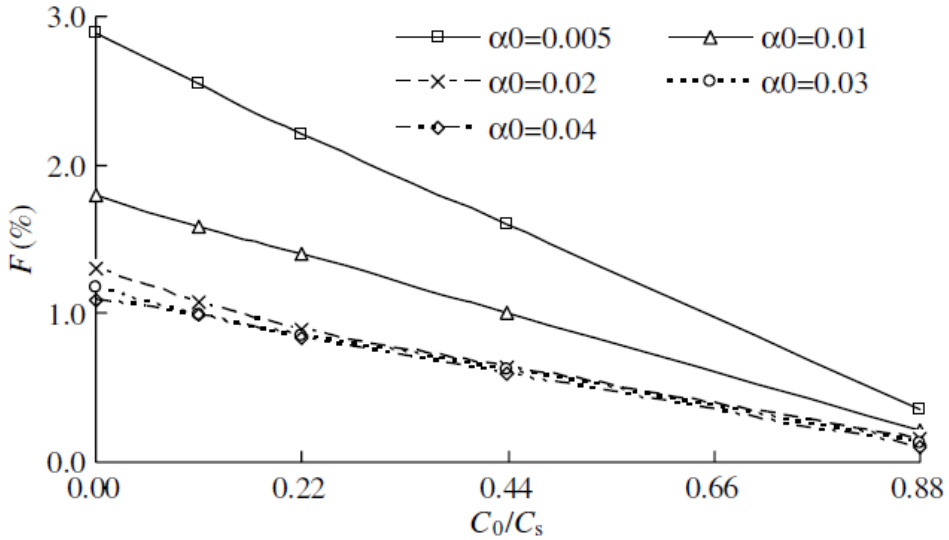

Figure 4.2.2.1: Relationship among oxygen absorption efficiency (F) and influencing factors: C_0/C_s (with $\Delta t = 20\ sec$) (Yin et al., 2012).

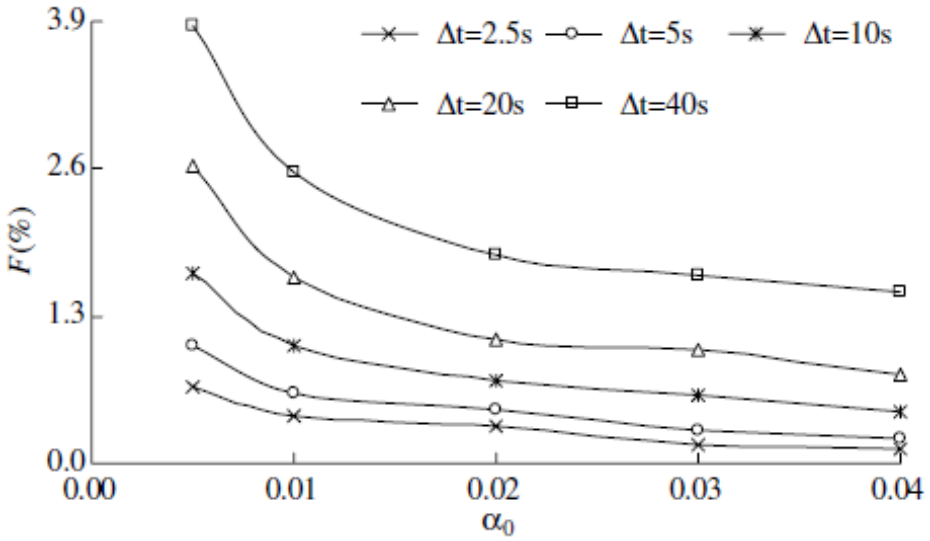

Figure 4.2.2.2: Relationship among oxygen absorption efficiency (F) and influencing factors: α_0 (with $C_0/C_s = 0.11$) (Yin et al., 2012).

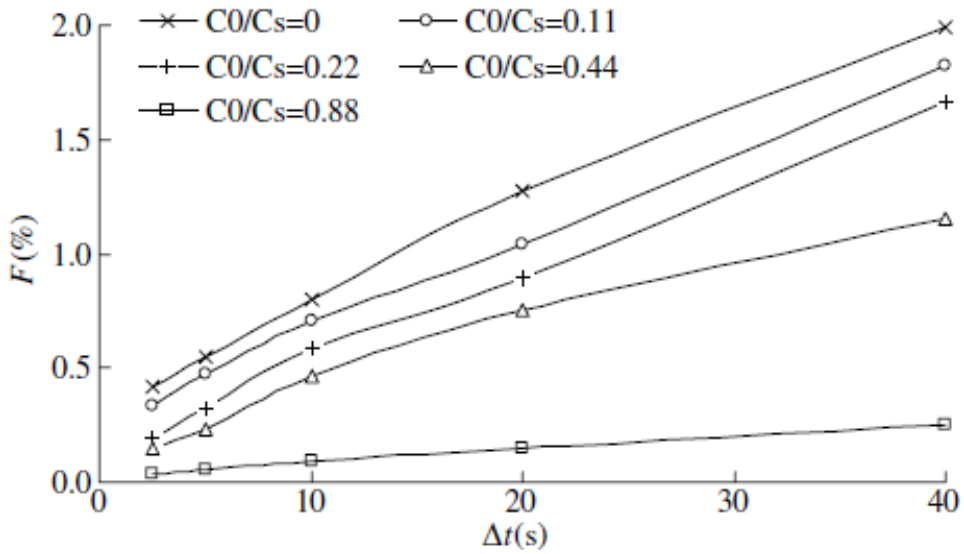

Figure 4.2.2.3: Relationship among oxygen absorption efficiency (F) and influencing factors: Δt (with $\alpha_0 = 0.02$) (Yin et al., 2012).

4.3 Dissolved Oxygen Concentration Measurements

4.3.1 Experimental Setup & Procedure

Water Supply Engineering Laboratory (WSEL) at SNU built an experimental setup for bubble generation and performed 15 experiments in order to investigate the effect of various parameters of pipe on DO concentration level within a cylinder filled with water. The schematic of the experimental setup is illustrated in Figure 4.3.1.1 and the parameters are listed in Table 4.3.1.1. The equipment used in the experiments consisted of two cylinders filled with water, an air controller, a pump, splitter with various dimensions, and a portable DO meter (Figure 4.3.1.2). The left cylinder supplied water at various velocities that ranged from 0.4 m/s to 1.2 m/s though the pump where the mixing process of water and air occurred. Air was supplied at various rates, keeping its volume fraction to be 0.1 for all the cases. The pipe length used in the experiments ranged from 6 m to 14 m and the diameter ranged from 2 mm to 10 mm. The running time for all the cases was 35 minutes.

At the start of the experiment, tap water and air were drawn into the generator by the suction power of the pump. The pump's impeller mixed water and air while they

were being injected into the pipe, and generated large bubbles. Then, the generated large bubbles were subjected to the shear force of the pipe, and broken down into smaller bubbles continuously until they became sufficiently fine. When the water containing the split bubbles were discharged from the outlet to the water in the right cylinder, the DO concentration was measured by the DO meter placed in the middle of the cylinder (Kim 2016).

Table 4.3.1.1: Parameters for each experiment case.

Set	Remark	L	D	V	Q_A/Q_W
1	D	6m	2mm	0.8m/s	0.1
			4mm		
			6mm		
			8mm		
			10mm		
2	V	6m	6mm	0.4m/s	0.1
				0.6m/s	
				0.8m/s	
				1.0m/s	
				1.2m/s	
3	L	6m	6mm	0.8m/s	0.1
		8m			
		10m			
		12m			
		14m			

Figure 4.3.1.1: Portable DO meter used for the experiments.

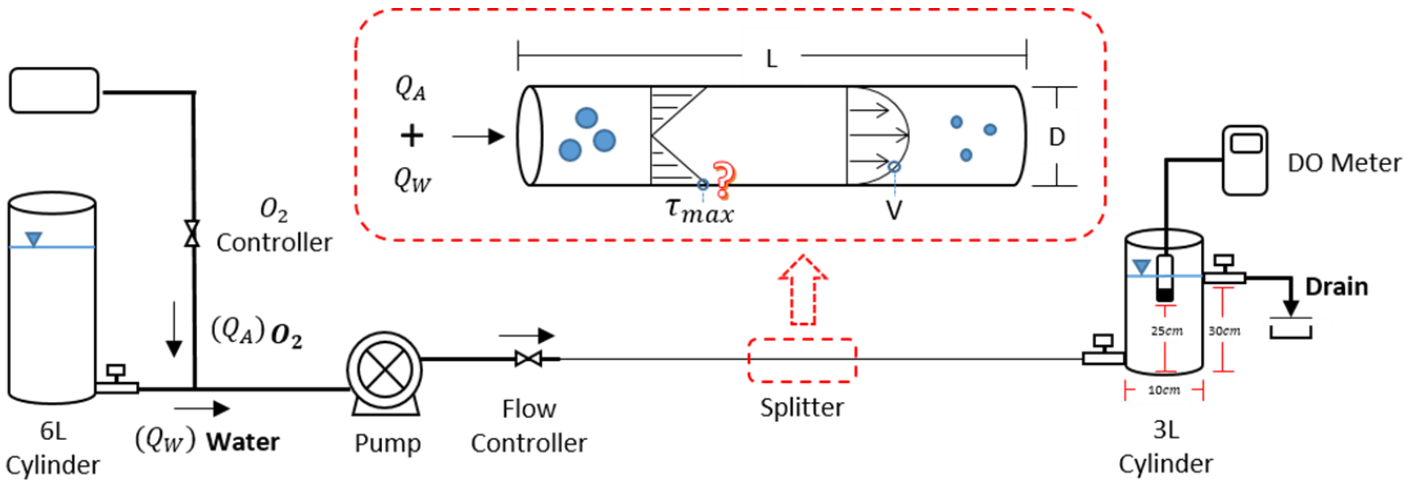

Figure 4.3.1.1: Schematic of the experimental setup.

4.3.2 Experimental Results

Table 4.3.2.1: Max DO concentration level for each case.

Set	Remark	L	D	V	Q_A/Q_W	DO_{max}
1	D	$6m$	$2mm$	$0.8m/s$	0.1	**42.21**
			$4mm$			**38.23**
			$6mm$			**27.34**
			$8mm$			**28.76**
			$10mm$			**26.74**
2	V	$6m$	$6mm$	$0.4m/s$	0.1	**15.85**
				$0.6m/s$		**26.45**
				$0.8m/s$		**27.34**
				$1.0m/s$		**29.47**
				$1.2m/s$		**34.56**
3	L	$6m$	$6mm$	$0.8m/s$	0.1	**27.34**
		$8m$				**32.27**
		$10m$				**32.60**
		$12m$				**35.93**
		$14m$				**40.28**

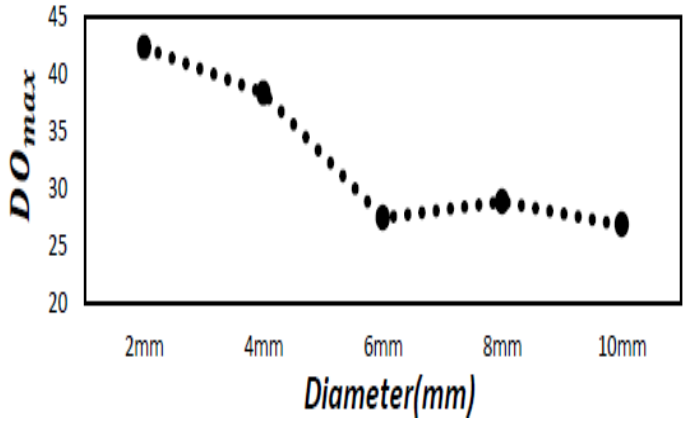

Figure 4.3.2.1: Relationship between DO concentration level and pipe diameter.

Figure 4.3.2.1 shows the effect of pipe diameter on the measured maximum DO concentration level. It can be observed that the increase in pipe diameter causes the decrease in maximum DO concentration level inside the right cylinder.

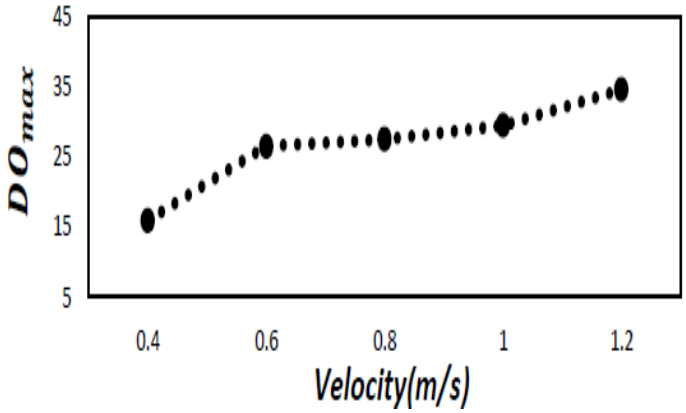

Figure 4.3.2.2: Relationship between DO concentration level and water velocity.

Figure 4.3.2.2 shows the effect of pipe's inlet water velocity on the measured maximum DO concentration level. It can be observed that the increase in inlet water velocity causes the decrease in maximum DO concentration level inside the right cylinder.

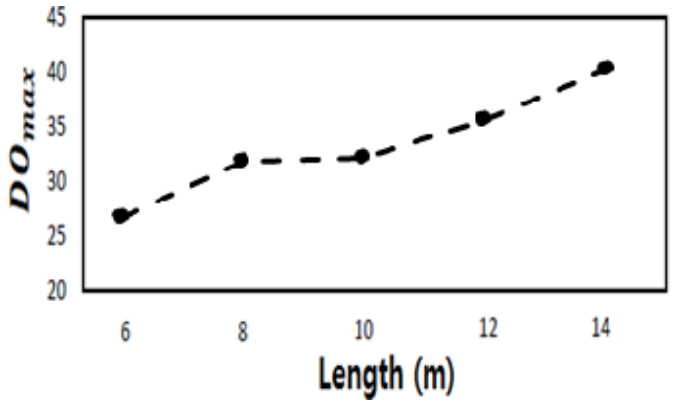

Figure 4.3.2.3: Relationship between DO concentration level and pipe length.

Figure 4.3.2.3 shows the effect of pipe length on the measured maximum DO concentration level. It can be observed that the increase in length causes the increase in maximum DO concentration level inside the right cylinder.

CHAPTER 5. NUMERICAL SIMULATION

5.1 Kocamustafaogullari and Wang (1991)

5.1.1 Computational Domain

Several numerical simulations were performed based on the experimental setup assigned by Kocamustafaogullari and Wang (1991). In order to do so a mesh was constructed as shown in Figure 5.1.1.1.

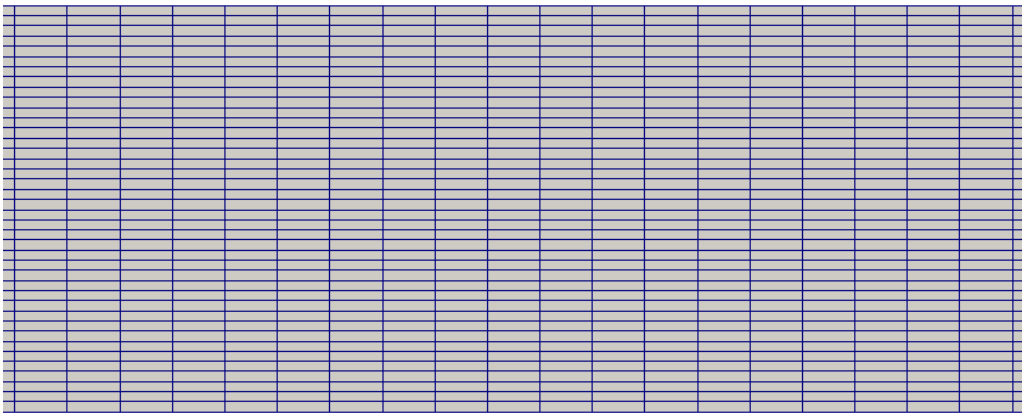

Figure 5.1.1.1: Computational domain constructed with Gmsh.

A 2-dimensional mesh to represent the straight pipe was constructed with a software called Gmsh, a finite element mesh generator with built-in pre- and post-processing facilities. The 2-dimensional geometry of the domain was assigned base on the dimensions depicted in Table 4.1.1.1. By performing numerous simulations and observing their relative error compared to the experimental data, it was determined that a total number of 143,141 grid points worked best. The cells are evenly distributed within the domain as shown in Figure 5.1.1.1.

5.1.2 Simulation Setup and Boundary Conditions

Local values of two-phase fluid's time-averaged axial Sauter mean diameter and axial water velocity components were computed. For the two-fluid model, numerical solutions to conservation of mass and momentum governing equations for each phase were obtained using OpenFOAM. Axial characteristics of bubbly flow structure was examined at the outlet of horizontal straight pipes. Details of the flow conditions within the bubbly flow regime are summarized in Tables 4.1.1.1, which were obtained from Kocamustafaogullari and Wang (1991).

IATE model was applied to predict the bubble size distribution of which the evaluation of the coalescence and breakup was performed by the utilization of a user subroutine incorporated within the CFD computer code. For IATE, four moments were adopted to explicitly track the distribution of bubble sizes ranging from 0 mm to 10 mm. For simplicity, all moments or bubbles classes in were assumed to travel in the same gas velocity which has been solved explicitly from the gas-phase of the two-fluid model.

Inlet conditions were assumed to be homogeneous with regards to the superficial water and gas velocities, void fractions for both phases and uniformly distributed bubble size in accordance with the flow conditions described in Table 4.1.1.1. At the pipe outlet, a relative average static pressure of zero was specified. For the reference case, the wall lubrication constants C_w1 and C_w2 were taken to have values of −0.01 and 0.05 as suggested by Antal et al. (1991). According to Ekambara et al. (2008), the lift and wall turbulent induced dispersion constants C_L and C_{TD} for horizontal pipe flow took on values of −0.2 and 0.5 respectively.

5.1.3 Simulations Results

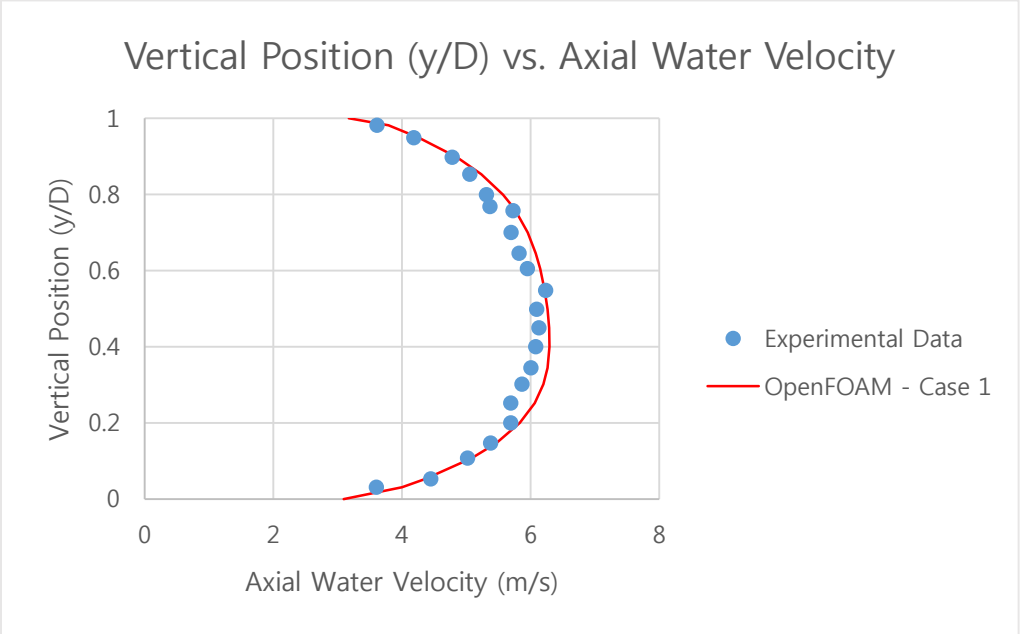

Figure 5.1.3.1: Comparison between experimental and numerical results, Case 1.

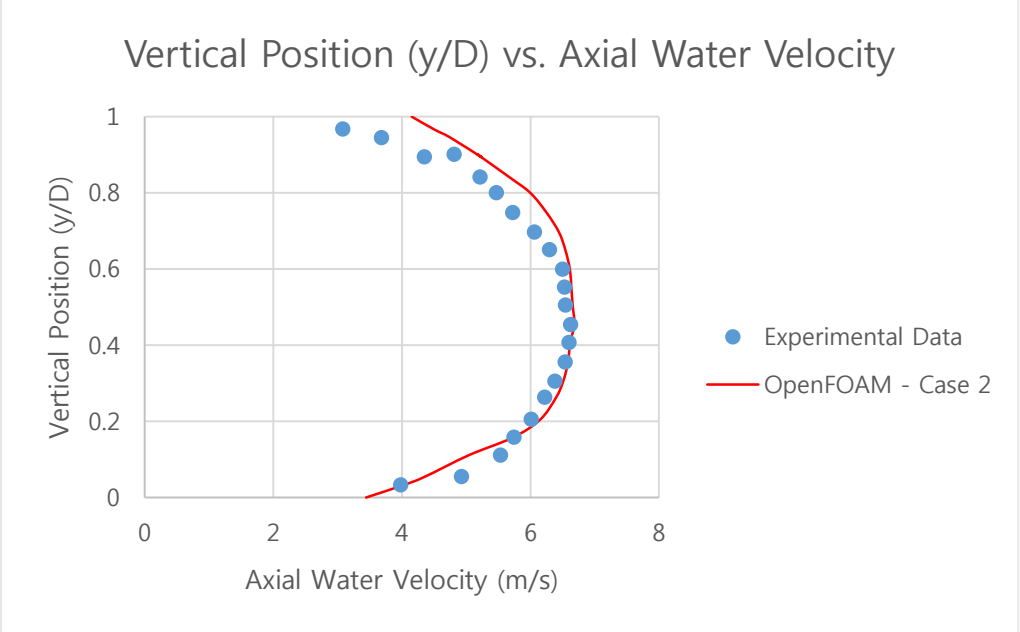

Figure 5.1.3.2: Comparison between experimental and numerical results, Case 2.

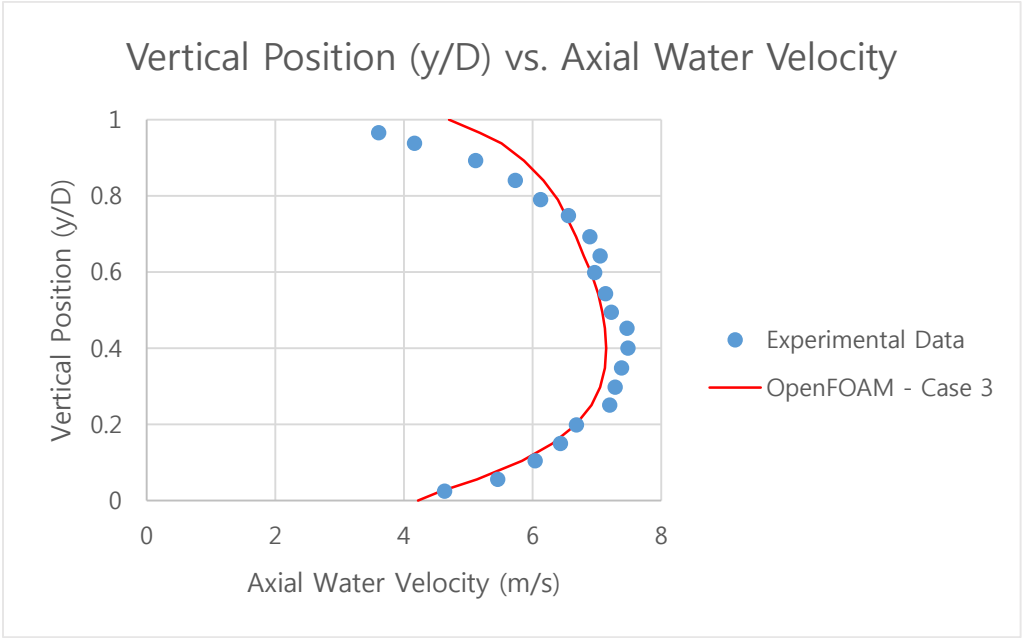

Figure 5.1.3.3: Comparison between experimental and numerical results, Case 3.

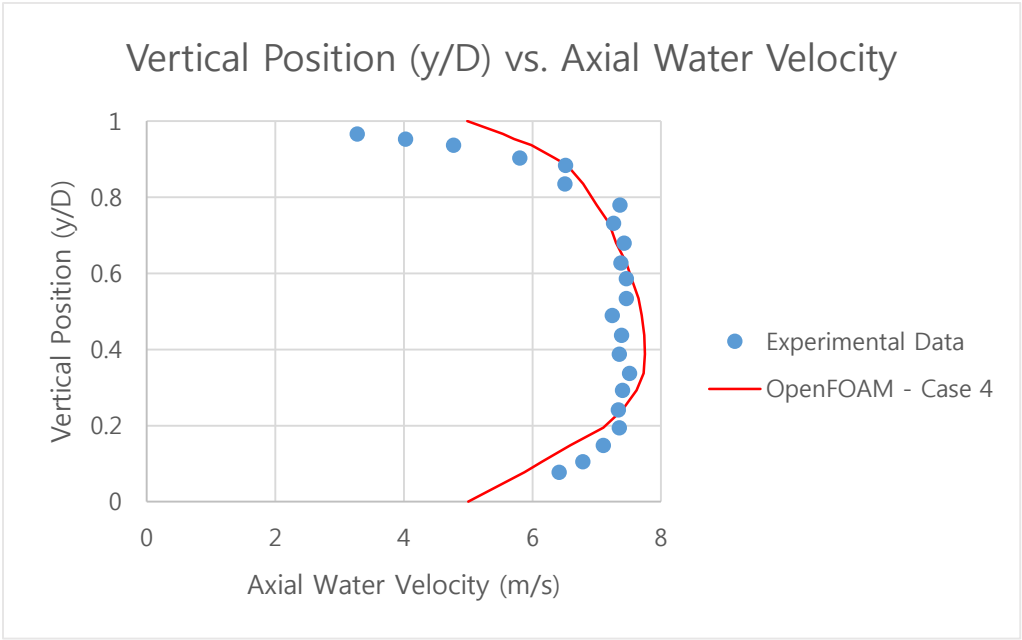

Figure 5.1.3.4: Comparison between experimental and numerical results, Case 4.

Figures 5.1.3.1 – 5.1.3.4 show the comparison of predicted and experimental data of axial liquid velocity profiles for different superficial gas and constant superficial liquid velocity. If only water phase was considered, the liquid velocity profile in the top region will be equal to the one in the bottom region, exhibiting a symmetry. But the results show that the axial water velocity profile is not symmetric due to the presence of gas in the flow. Referring to Figures 5.1.3.1 – 5.1.3.4, the liquid velocity in the upper region of the pipe is slightly lower than in the lower region for higher gas velocity. The model prediction of axial liquid velocity shows the relative mean and maximum errors to be ±4% and ±15%, respectively.

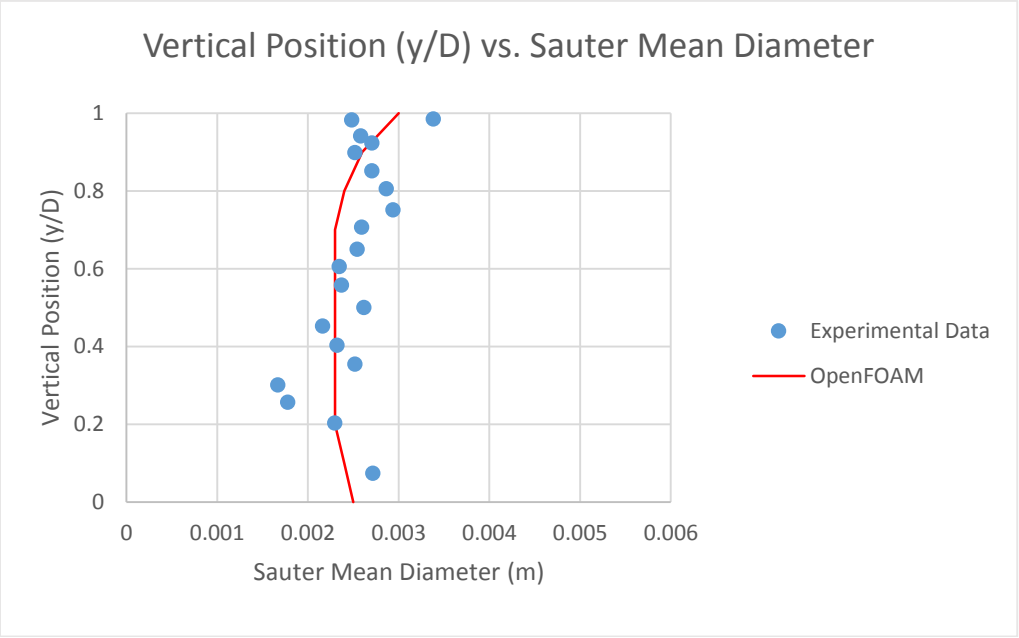

Figure 5.1.3.5: Comparison between experimental and numerical results, Case 1.

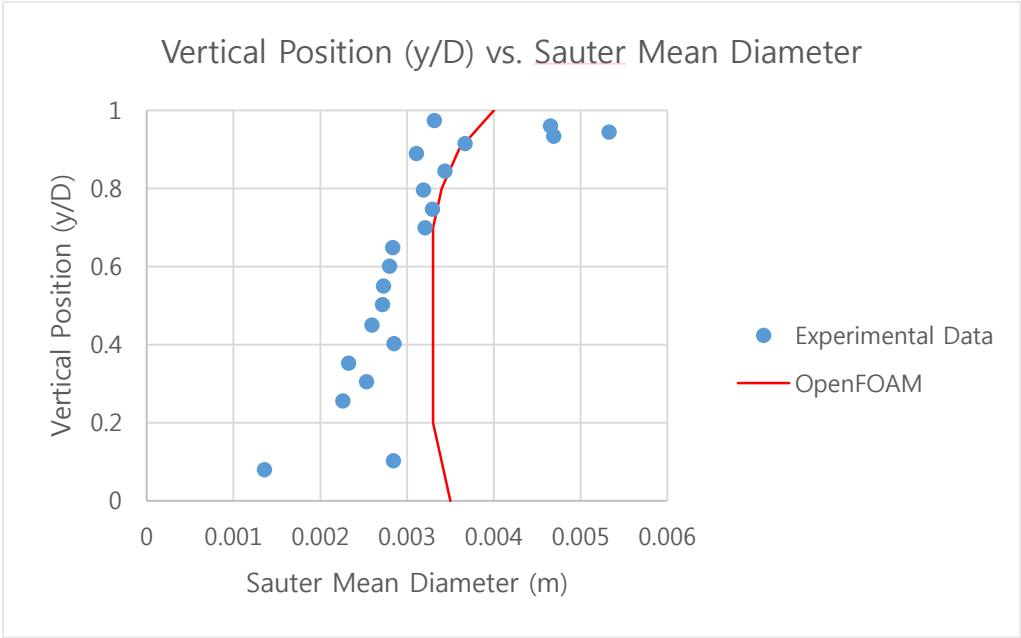

Figure 5.1.3.6: Comparison between experimental and numerical results, Case 2.

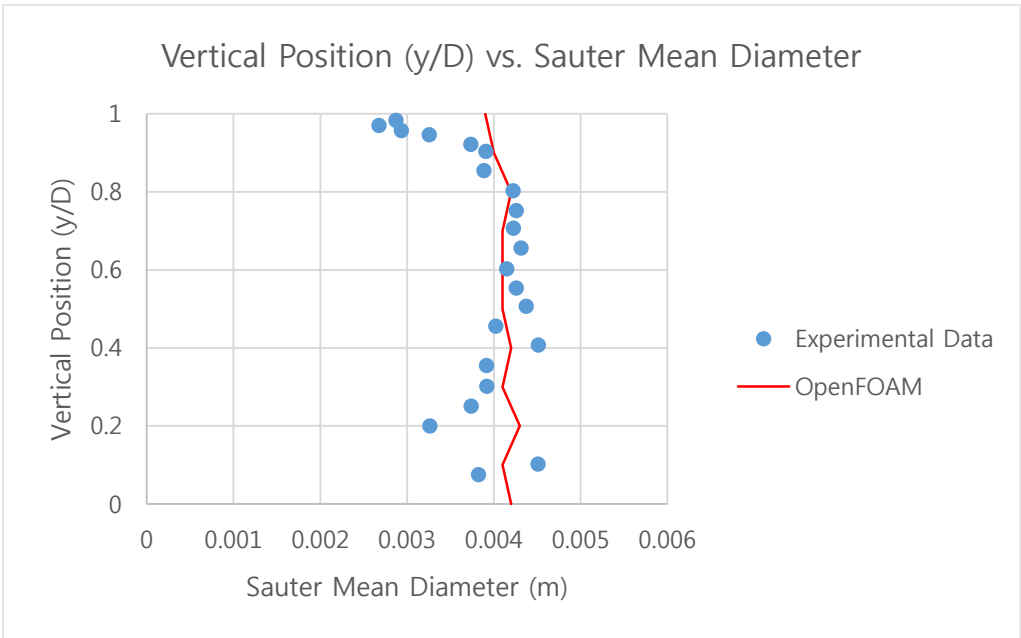

Figure 5.1.3.7: Comparison between experimental and numerical results, Case 3.

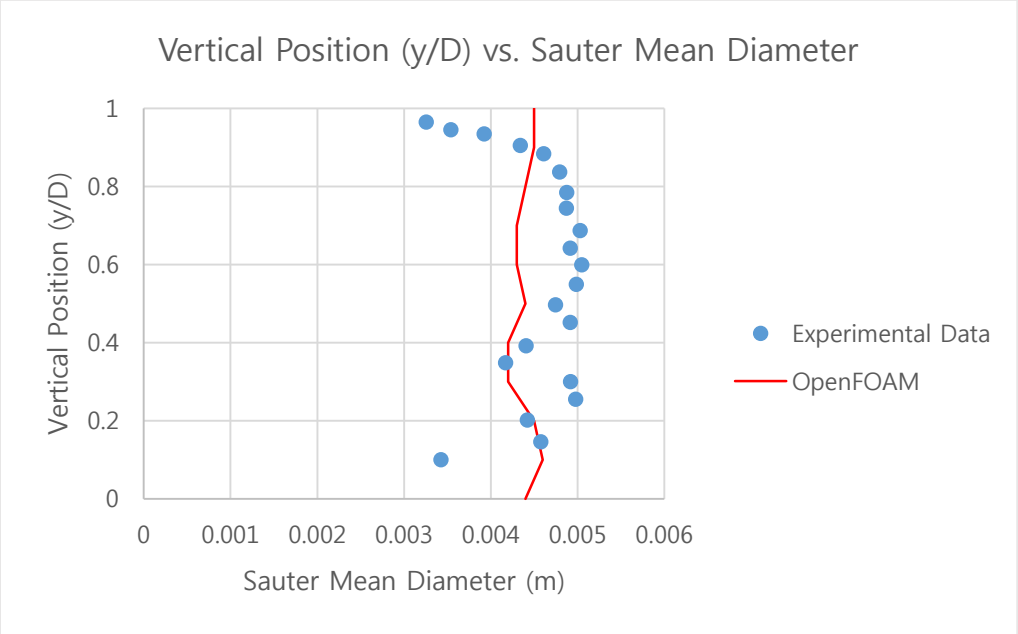

Figure 5.1.3.8: Comparison between experimental and numerical results, Case 4.

Figures 5.1.3.5 – 5.1.3.8 show the comparison of predicted and experimental data of axial Sauter mean diameter profiles for different superficial gas and constant superficial liquid velocities. The bubble size distribution was determined while considering the bubble coalescence and breakup phenomena. Bubble coalescence and breakup are primarily influenced by the local gas volume fraction. Because of the non-uniform profiles of the gas volume fraction and dissipation rate, the bubble size distribution varies with the position as well. The model prediction of axial Sauter mean diameter shows the relative mean and maximum errors to be ±8% and ±30%, respectively.

The experimental and simulated results indicate that the volume fraction reaches its maximum value near the upper pipe wall. It was observed that the mean bubble diameter ranged from 1.5 to 5 mm, depending on the location and flow conditions. It was also found that increasing the gas flow rate while keeping water flow rate constant would increase the local volume fraction. The simulation results were consistent with experimental observed from the experiments. Figure 5.1.3.9 shows the numerical results

of the highest wall shear stress occurred due to water flow for each case. From the figure it can be determined that Case 1 produced the highest wall shear stress and Case 4, the lowest.

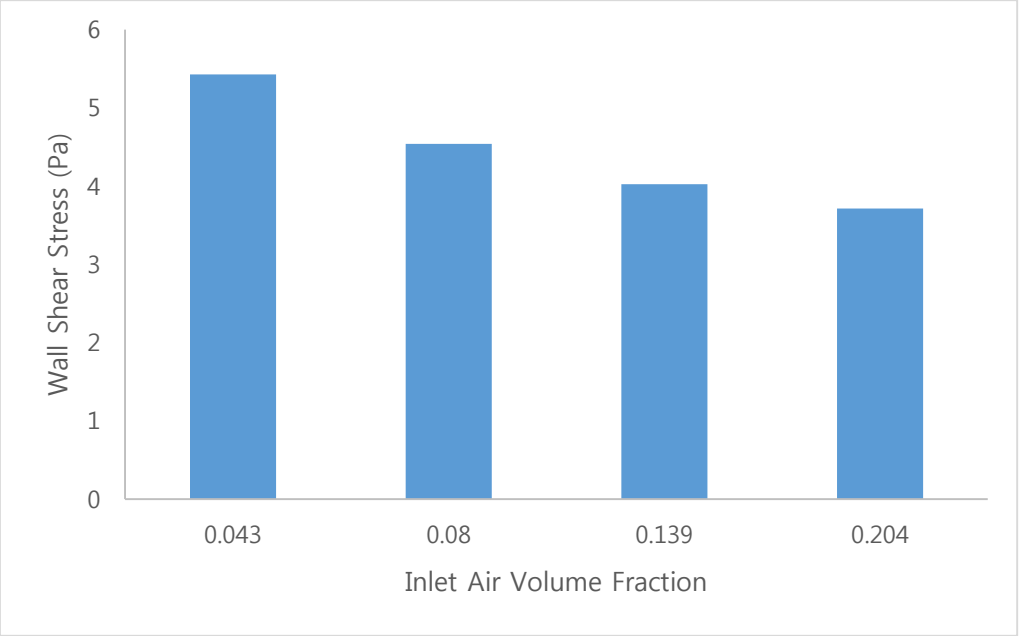

Figure 5.1.3.9: Wall shear stress values obtained from numerical simulations, Case 1 – Case 4.

5.2 Water Supplying Engineering Lab: Simulation

5.2.1 Simulations Results

Table 5.2.1.1: Wall shear stress values obtained using OpenFOAM for Case 1 - 5.

Case	L (m)	D (m)	V (m/s)	Reynold's Number	Flow Type	Solver Type	Wall Shear Stress (Pa)
1	6	0.002	0.8	1600	Laminar	Turbulent	4.16
2	6	0.004	0.8	3200	Transient	Turbulent	3.06
3	6	0.006	0.8	4800	Turbulent	Turbulent	2.70
4	6	0.008	0.8	6400	Turbulent	Turbulent	2.47
5	6	0.01	0.8	8000	Turbulent	Turbulent	2.31

Table 5.2.1.2: Wall shear stress values obtained using OpenFOAM for Case 6 - 7.

Case	L (m)	D (m)	V (m/s)	Reynold's Number	Flow Type	Solver Type	Wall Shear Stress (Pa)
6	6	0.006	0.4	2400	Transient	Turbulent	0.90
7	6	0.006	0.6	3600	Turbulent	Turbulent	1.70
8	6	0.006	0.8	4800	Turbulent	Turbulent	2.70
9	6	0.006	1	6000	Turbulent	Turbulent	3.90
10	6	0.006	1.2	7200	Turbulent	Turbulent	5.30

Table 5.2.1.3: Wall shear stress values obtained using OpenFOAM for Case 11 – 15.

Case	L (m)	D (m)	V (m/s)	Reynold's Number	Flow Type	Solver Type	Wall Shear Stress (Pa)
11	6	0.006	0.8	4800	Turbulent	Turbulent	2.70
12	8	0.006	0.8	4800	Turbulent	Turbulent	2.70
13	10	0.006	0.8	4800	Turbulent	Turbulent	2.70
14	12	0.006	0.8	4800	Turbulent	Turbulent	2.70
15	14	0.006	0.8	4800	Turbulent	Turbulent	2.70

Tables 5.2.1.1 – 5.2.1.3 show the numrical wall shear stress values for Case 1-15. In Table 5.2.1.1, the pipe diameter is set as a variable and as shown in the table and Figure 5.2.1.1, the wall shear stress values decrease as the diameter increases. In Table 5.2.1.2, the inlet water velocity is set as a variable and as shown in the table and Figure 5.2.1.2, the wall shear stress values increase as the water velocity increases. And finally, in Table 5.2.1.3, the pipe length is set as a variable and as shown in the table and Figure 5.2.1.3, the wall shear stress values is constant for all the cases.

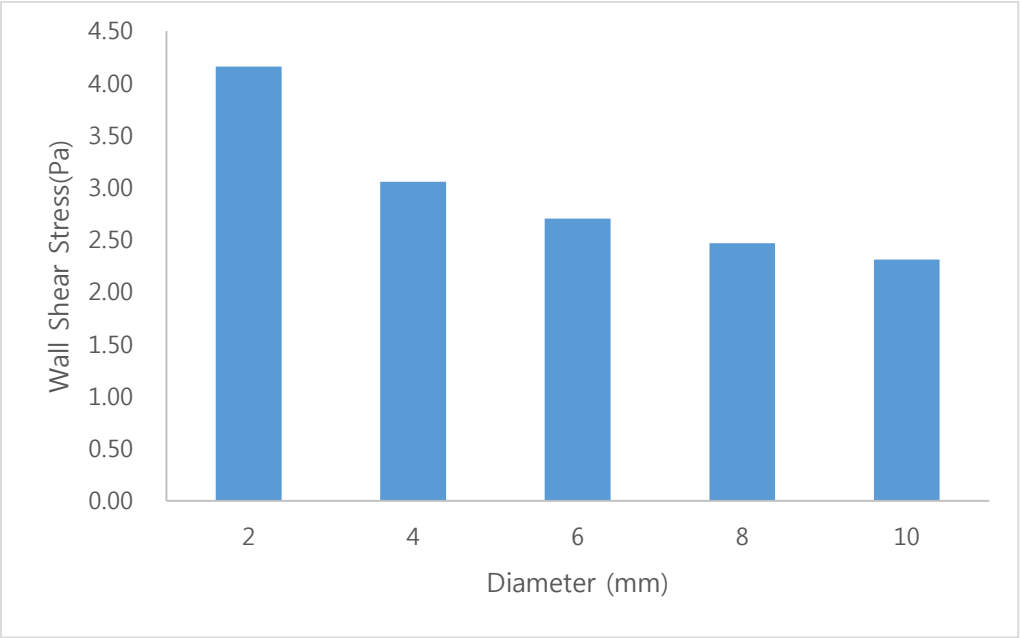

Figure 5.2.1.1: Wall shear stress versus pipe diameter.

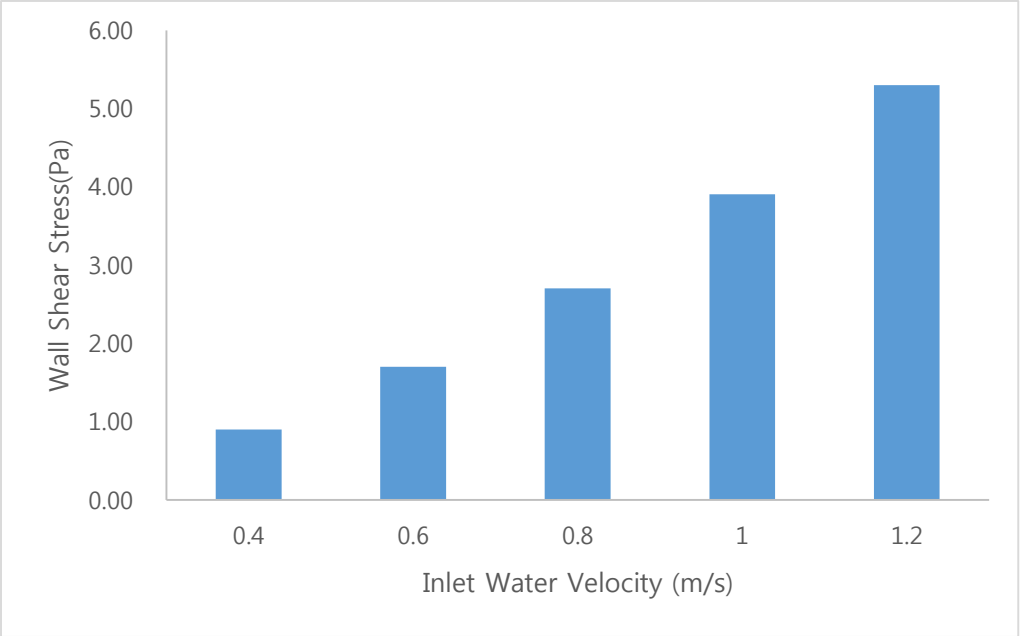

Figure 5.2.1.2: Wall shear stress versus inlet water velocity.

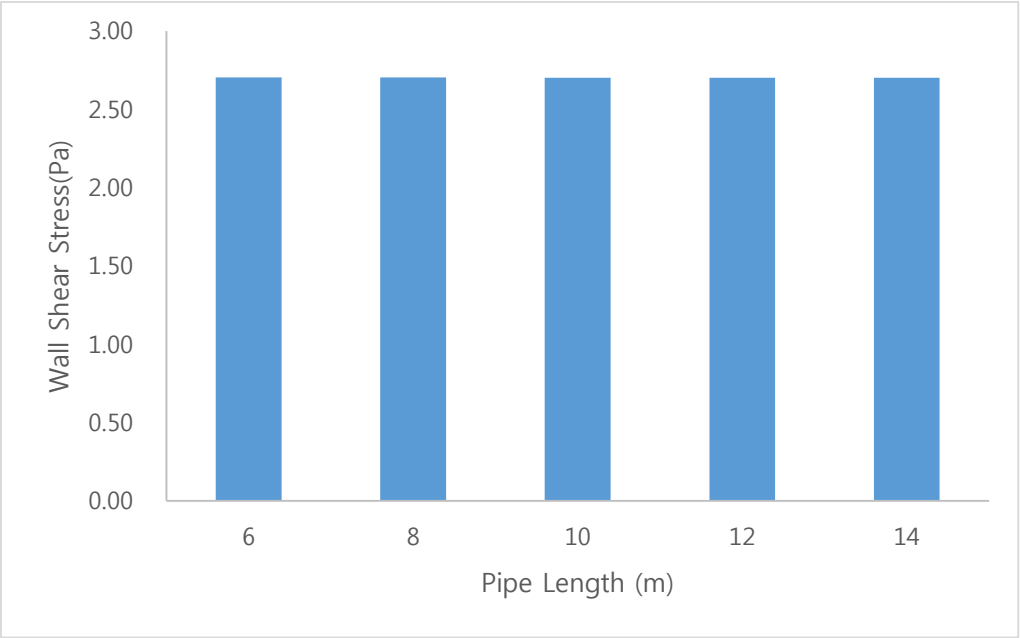

Figure 5.2.1.3: Wall shear stress versus pipe length.

CHAPTER 6. DISCUSSION

In this chapter, all the experimental and numerical results mentioned previously are compared to each other and the effect of pipe wall shear stress on DO concentration is discussed.

Before going into the discussion part. We have to keep in mind the fundamental idea of this study, which is that, fine bubbles have a higher mass transfer when the diameter of the bubble gets smaller (Kim, 2010) and smaller bubbles are more capable of enhancing DO concentration level (Yin et al., 2012). In other words, high DO concentration level means the presence of smaller bubbles inside horizontal pipe. In this study, the pipe wall shear stress is considered to be the major factor for causing smaller bubbles and thus, high DO concentration level. And the fundamental idea of determining the possible impacts of pipe wall shear stress are to look into its relationship with velocity gradient near wall.

Based on the experimental results obtained by Kocamustafaogullari and Wang (1991), the numerical simulations were carried out and the pipe wall shear stress was computed for each case. Figure 5.1.2.9 shows the pipe wall shear stress values for each case. From the figure it can be determined that Case 1 produced the highest wall shear stress and Case 4, the lowest. When Figures 5.1.3.5 – 5.1.3.8 are observed, the Sauter mean diameter values indicate that Case 1 produced the smallest air bubbles while, Case 4 produced the largest.

Yin et al.'s (2012) numerical and experimental results are shown in Figures 4.2.2.1 – 4.2.2.3. The pipe wall shear stress was not directly considered during the experiments. Bur from the results, it can be argued that the pipe wall shear stress might have played a key role. Figure 4.2.2.1 and Figure 4.2.2.2 show that the oxygen efficiency was measured and simulated to be highest when the inlet air volume fraction was lowest. From Kocamustafaogullari and Wang's (1991) results, we could see that as the inlet air volume fraction became smaller, the pipe wall shear stress increased.

Figures 4.2.2.3 and 4.3.2.3 show the similar trend. As the pipe length increased, DO concentration increased as well. The reasons are that when the length increases,

there is much more time to transfer oxygen from the bubbles to the water and much more time for bubbles breakup due to wall shear stress.

Based on the experimental and numerical results mentioned above, 16 plots (Figure 6.1 – 6.16, see below) were constructed for comparison and 5 sets of arguments were made and they are the followings:

1. Using Figures 6.1 and 6.2, the following arguments could be made:
   Pipe diameter increases → velocity gradient near wall decreases → wall shear stress decreases → bubble size increases → maximum DO concentration decreases.
2. Using Figures 6.3 - 6.6, the following arguments could be made:
   Inlet air volume fraction increases → viscosity of two-phase flow decreases → wall shear stress decreases → bubble size increases → oxygen absorption efficiency decreases.
3. Using Figures 6.7 - 6.10, the following arguments could be made:
   Pipe length increases → more time for oxygen transfer and more time for bubbles to breakup due to wall shear stress → oxygen absorption efficiency increases → maximum DO concentration increases.
4. Using Figures 6.11 and 6.12, the following arguments could be made:
   Inlet water velocity increases → velocity gradient near wall increases → wall shear stress increases → bubble size decreases → maximum DO concentration increases.
5. Using Figures 6.13 - 6.16, the following arguments could be made:
   Inlet air velocity/volume fraction increases → viscosity of two-phase flow and velocity gradient near wall decrease→ wall shear stress decreases → bubble size increases → oxygen absorption efficiency decreases.

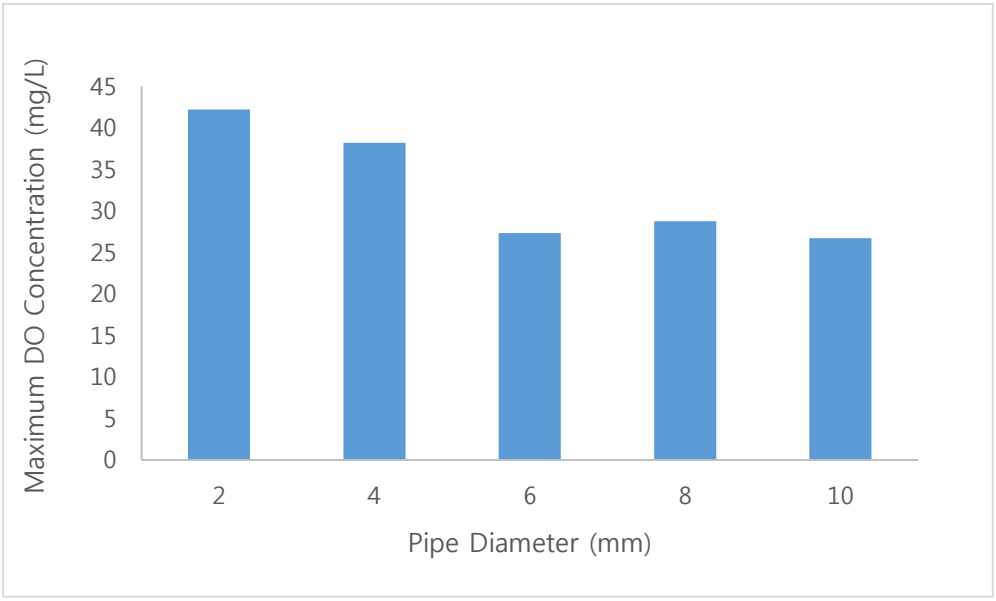

Figure 6.1: Maximum DO concentration versus pipe diameter.

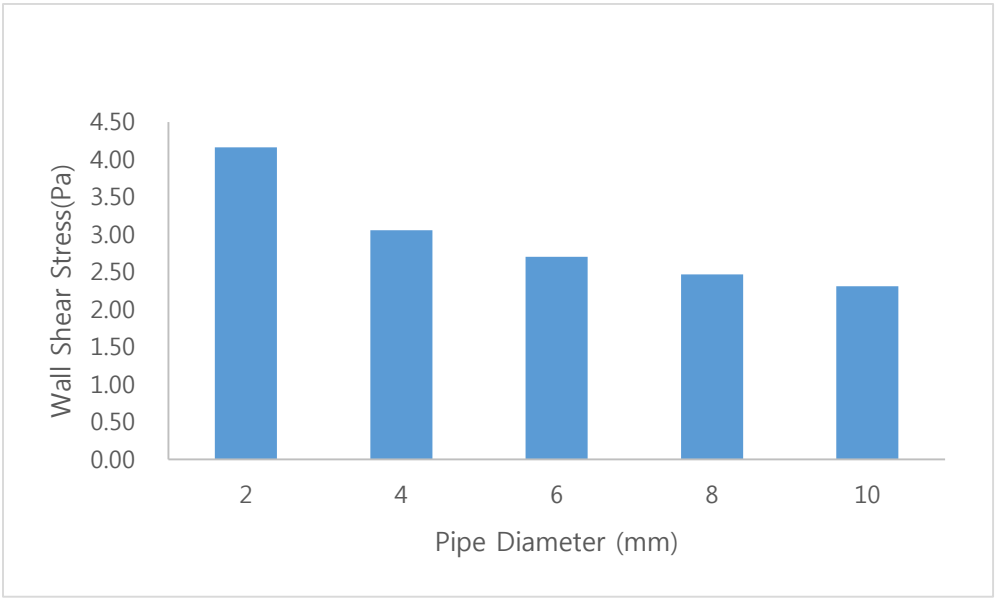

Figure 6.2: Wall shear stress versus pipe diameter.

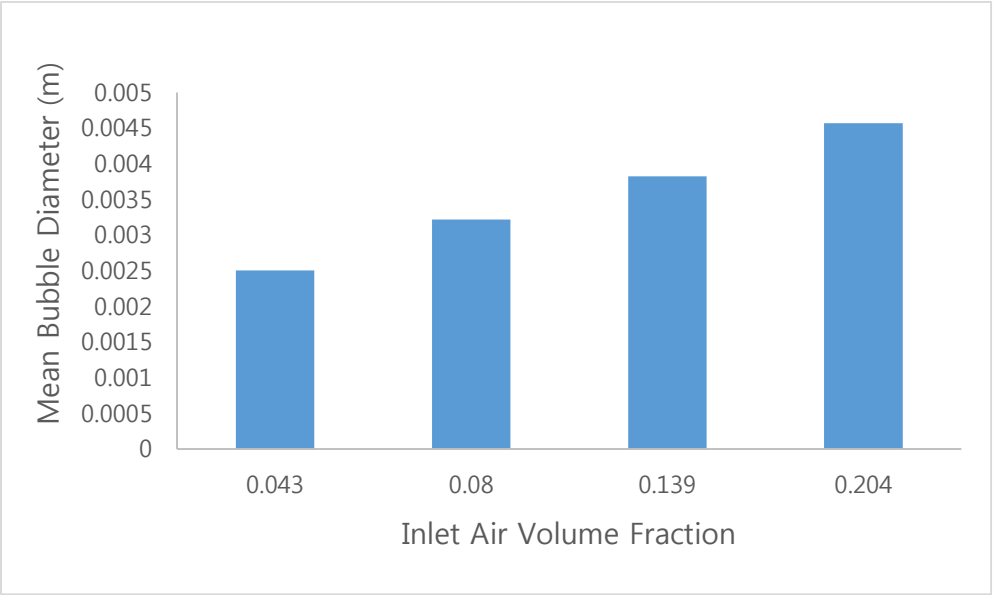

Figure 6.3: Mean bubble diameter versus inlet air volume fraction.

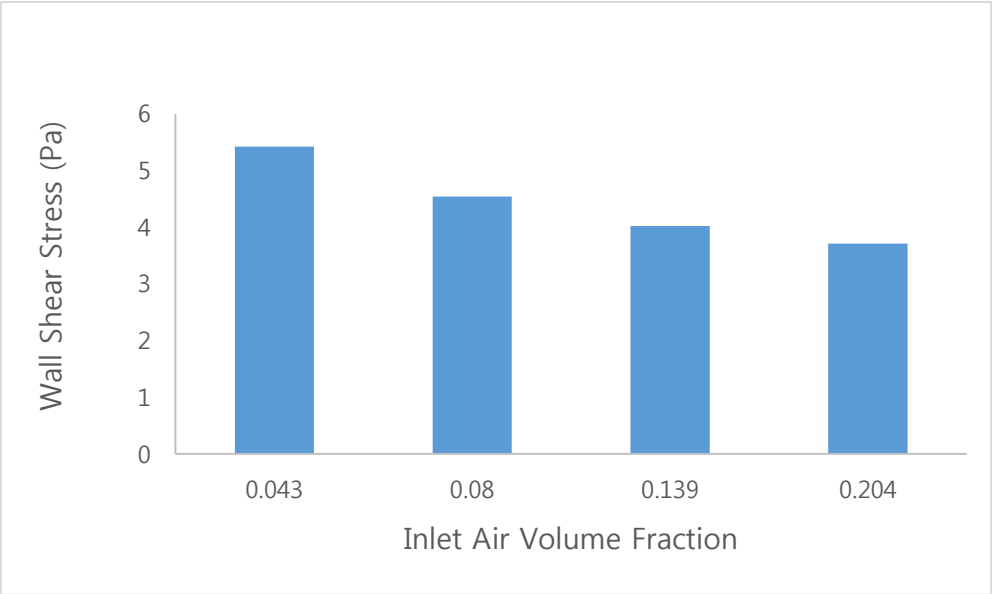

Figure 6.4: Wall shear stress versus inlet air volume fraction.

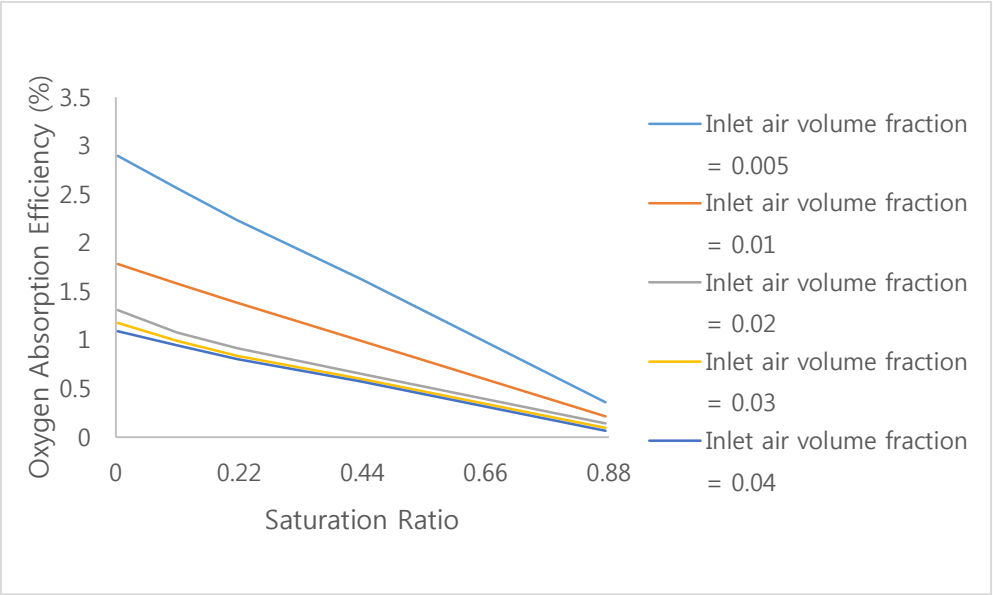

Figure 6.5: Oxygen absorption efficiency versus saturation ratio.

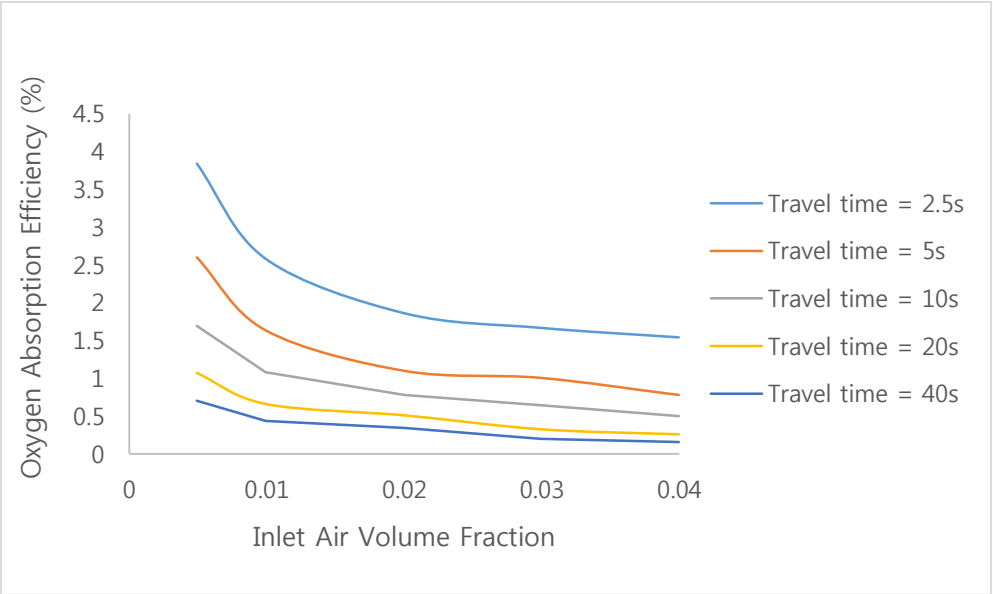

Figure 6.6: Oxygen absorption efficiency versus inlet air volume fraction.

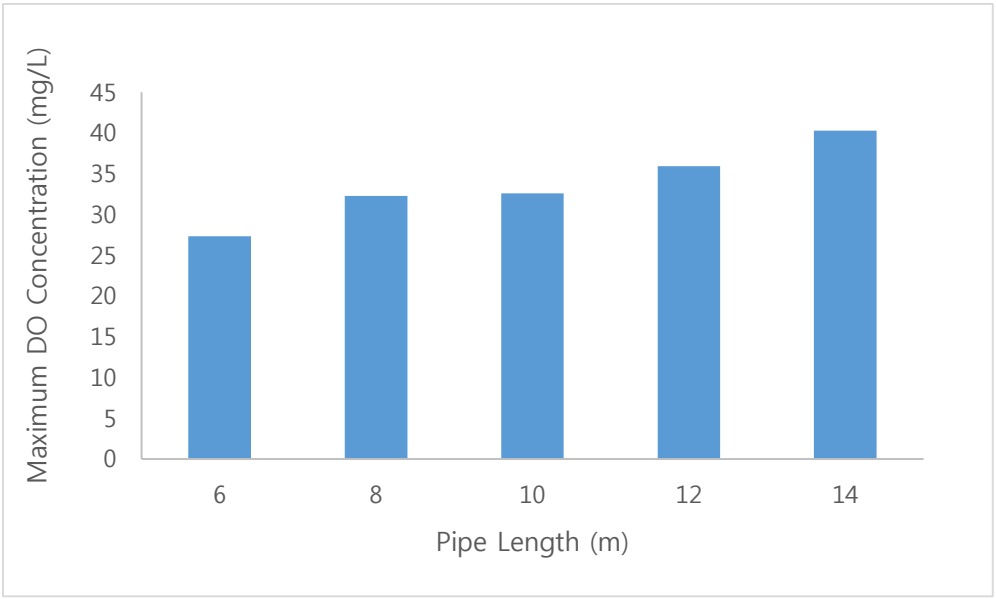

Figure 6.7: Maximum DO concentration versus pipe length.

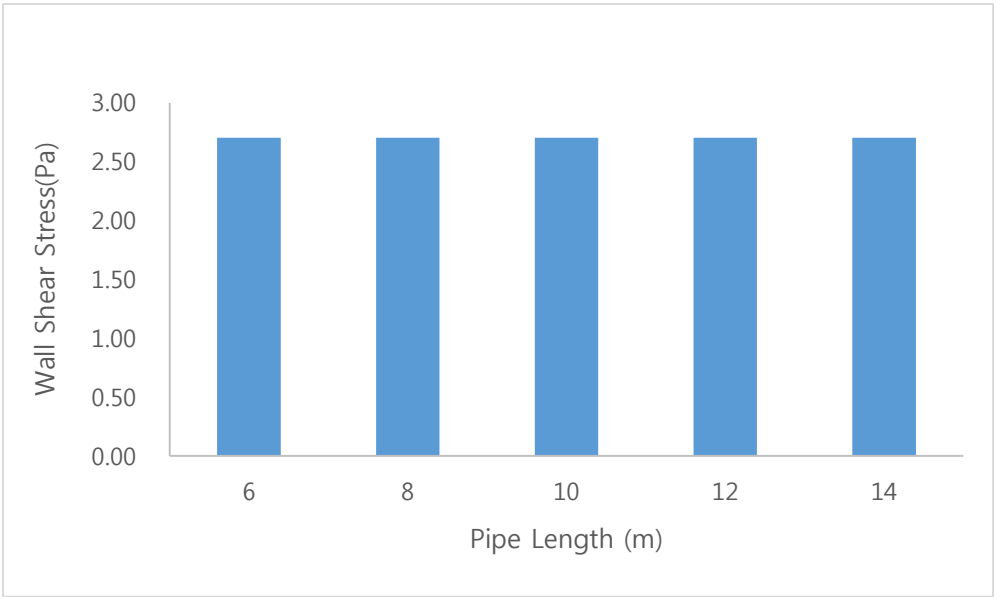

Figure 6.8: Wall shear stress versus pipe length.

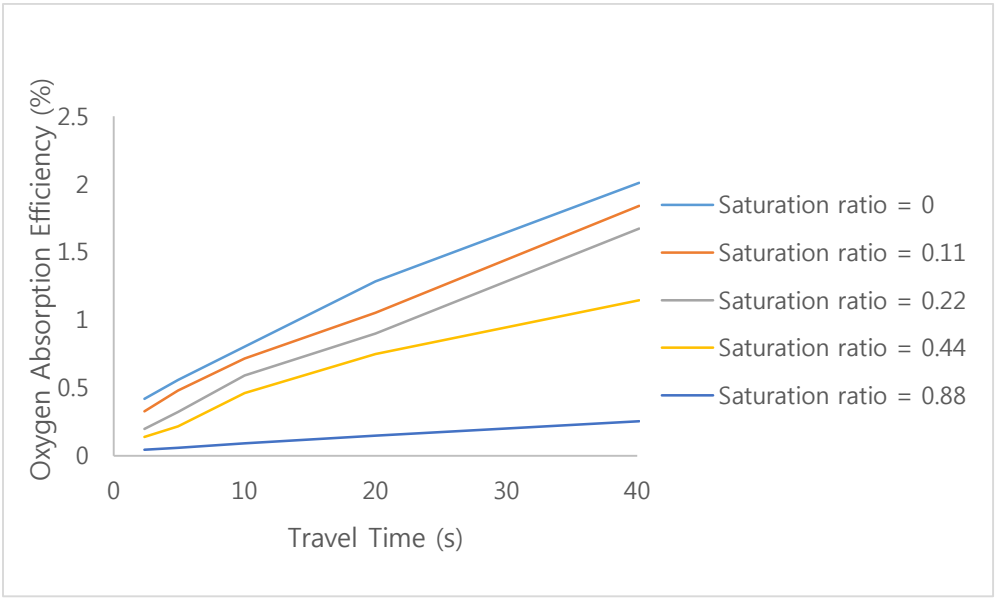

Figure 6.9: Oxygen absorption efficiency versus travel time.

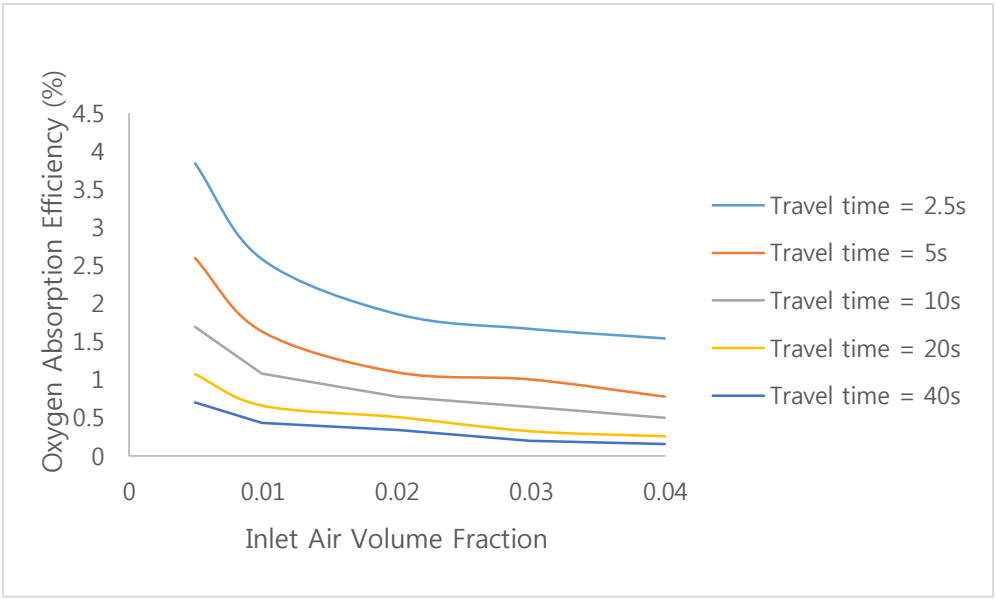

Figure 6.10: Oxygen absorption efficiency versus inlet air volume fraction.

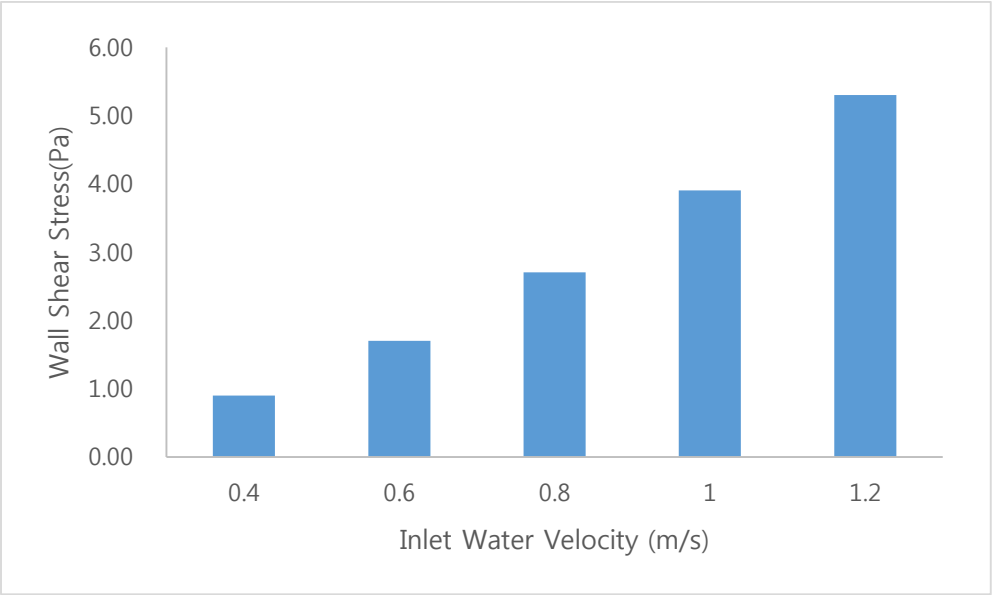

Figure 6.11: Wall shear stress versus inlet water velocity.

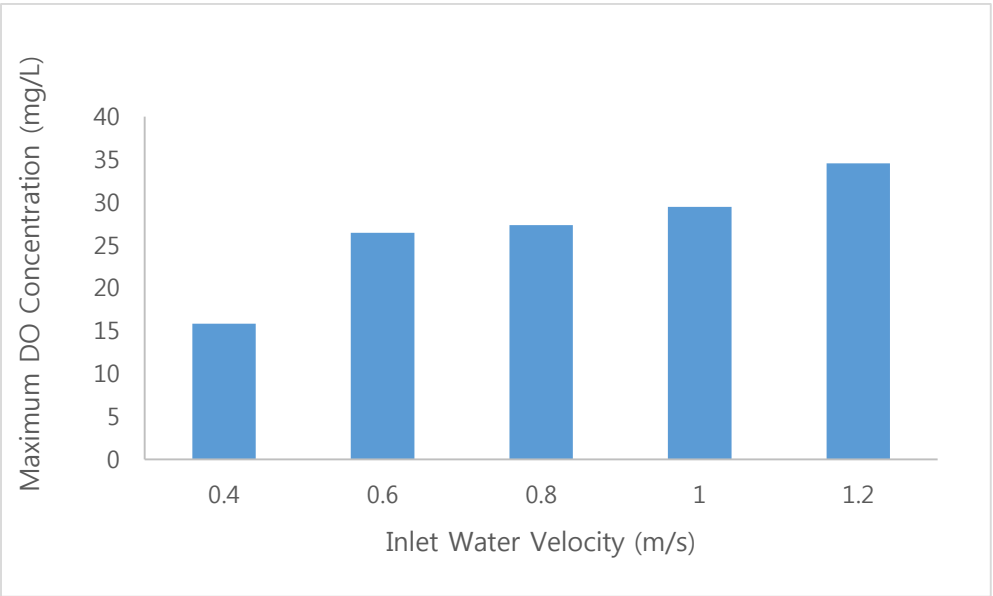

Figure 6.12: Maximum DO concentration versus inlet water velocity.

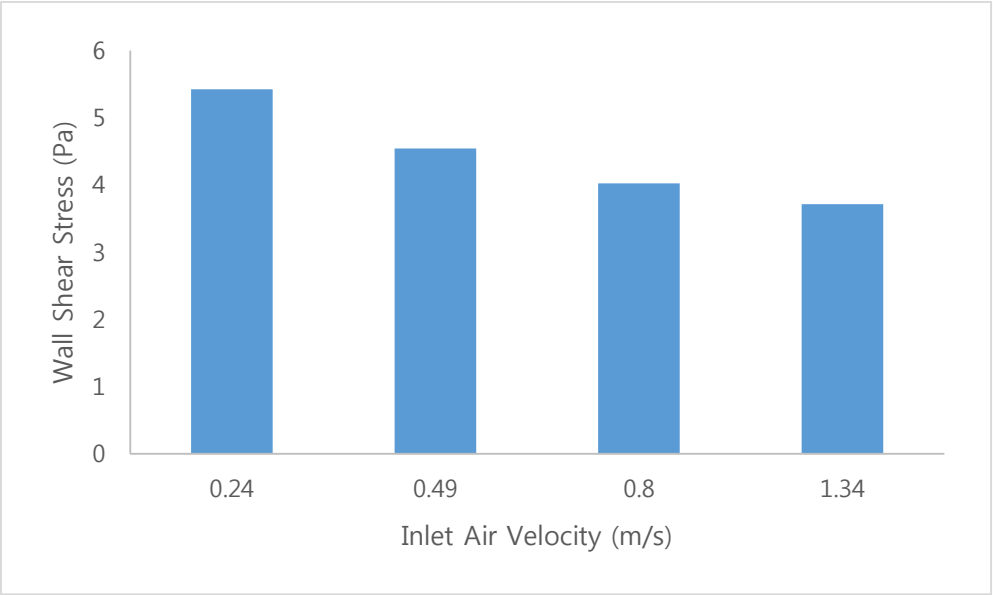

Figure 6.13: Wall shear stress versus inlet air velocity.

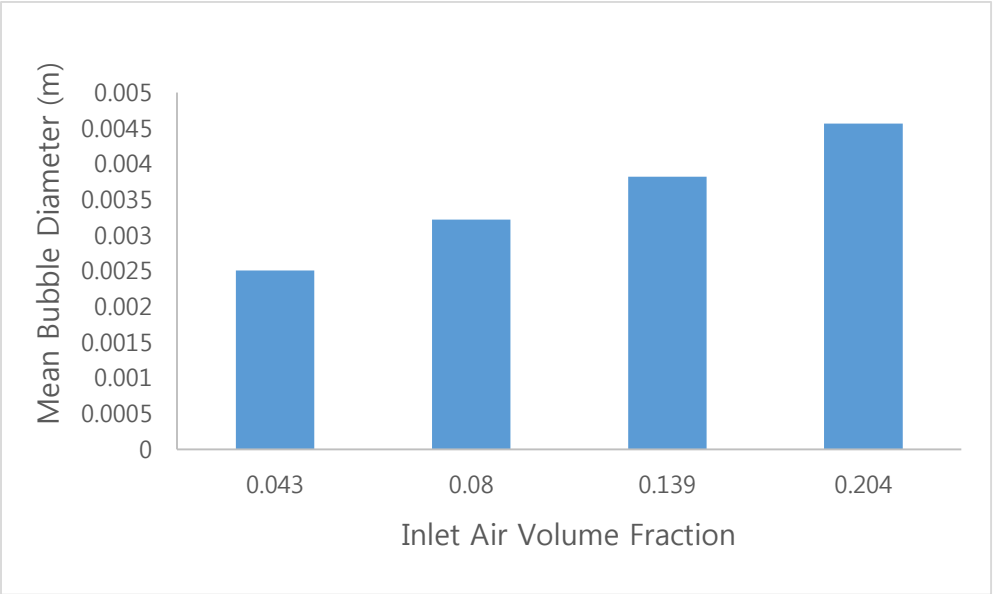

Figure 6.14: Mean bubble diameter versus inlet air volume fraction.

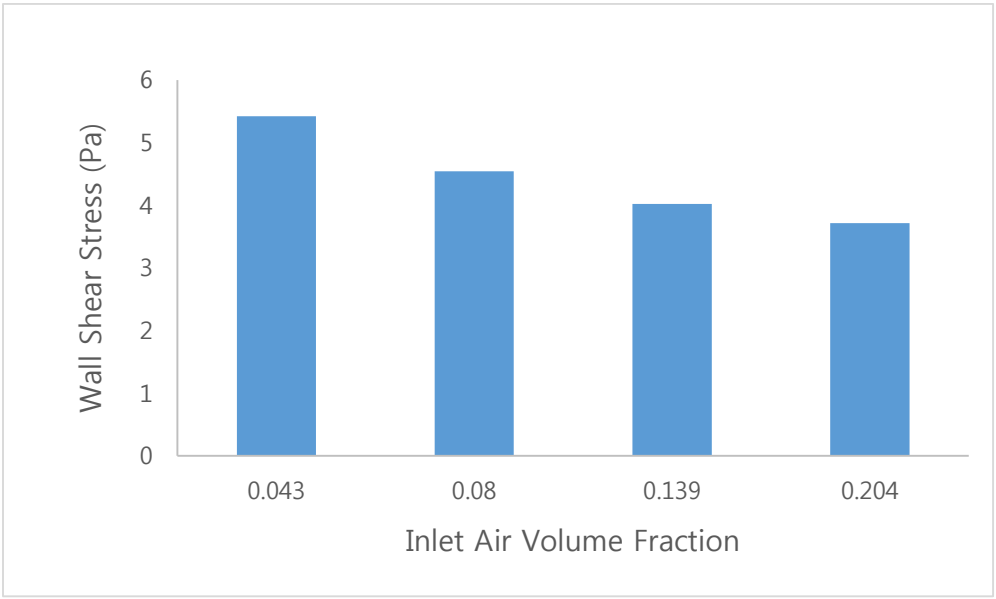

Figure 6.15: Wall shear stress versus inlet air volume fraction.

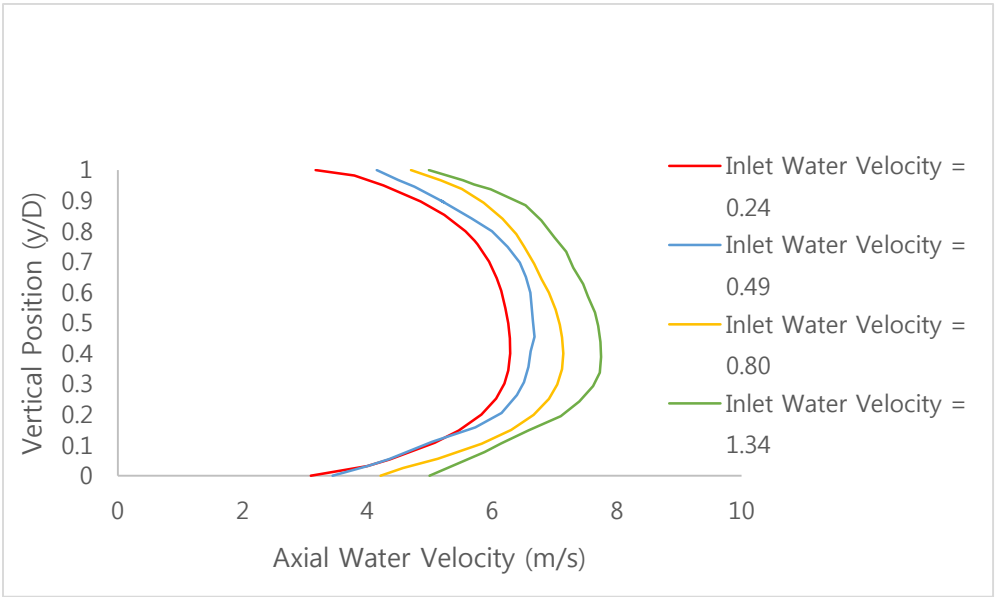

Figure 6.16: Axial water velocity profiles.

CHAPTER 7. CONCLUSION

Detailed comparisons between the CFD simulations and experimental data reported by Kocamustafaogullari and Wang (1991), Yin et al. (2012), and WSEL were presented. Good agreement was seen between the predicted and the experimental data of the Sauter mean bubble diameter and liquid velocity for a range of superficial gas (0.25 to 1.34 m/s) and water (5.1m/s) velocities and volume fraction (4 to 21%). The relative error between the predicted and the experimental data of the water velocity and Sauter mean bubble diameter ranged from 4% to nearly 15% and 8% to 30%.

Our theory claiming that pipe wall shear stress might play a key role in affecting bubble size and DO concentration, turned out to be reasonable. Considering the results obtained by Yin et al (2012), Kocamustafaogullari and Wang (1991), Water Supply Engineering Laboratory, and CFD simulations, the following conclusions were made:

1. Once the inlet air volume decreases, the change in near wall water velocity is insignificant while the internal velocity of water decreases notably. Because of this phenomenon, the water velocity gradient near wall increases causing the increase in wall shear stress and decrease in bubble size. And finally DO concentration increases.
2. Once the pipe length increases, the travel time of air-water mixture increases, allowing more time for the oxygen to transfer to the water and more time for the bubbles to breakup into smaller bubbles due to wall shear stress. And eventually, DO concentration increases.
3. Once the water velocity increases, the wall shear stress increases as well and eventually DO concentration increases.
4. When comparing all the experimental and numerical results, the effect of wall shear stress on bubbles size and DO concentration could be determined. And finally, we came to a conclusion that high pipe wall shear stress will produce high DO concentration level within a body of water.

CHAPTER 8. REFERENCES

Andreussi, P., Paglianti, A., Silva, F.S., 1999. Dispersed bubble flow in horizontal pipes. Chem. Eng. Sci. 5, 1101–1107.

Andritsos, and T. J., Hanratty. Influence of interfacial waves in stratified gas-liquid flows. AIChE J.1987, 33: 444-454.

Agrawal, S. (2013). Bubble dynamics and interface phenomenon. Journal of Engineering and Technology Research J. Eng. Technol. Res., 5(3), 42-50. doi:10.5897/jetr2013.0297

Brennen, C. E. (2005). Fundamentals of multiphase flow. Cambridge: Cambridge University Press.

Camp, T.R., 1963. Water and its Impurities. 2nd Edn., Reinhold Publishing Co., New York, USA.

Çengel, Y. A., & Cimbala, J. M. (2010). Fluid mechanics: Fundamentals and applications. Boston, Mass.: McGraw-Hill.

Chesters, A.K., 1991. The modeling of coalescence processes in fluid liquid dispersions – a review of current understanding. Chem. Eng. Res. Des. 69, 259–270.

Cognet, M. Leboucrm and M.Souhar. Wall shear stress measurements by electrochemical probe for gas-liquid two-phase flow in vertical duct, AIChE J. 1984, 30:338-341.

Cravarolo, A.Giorgini, A. Hassid and E.Pedrocchi. A device for the measurement of shear stress on the wall of a conduit-its application in the mean density determination

in two-phase flow shear stress data in two-phase adiabatic vertical flow. CISE (Milan). 1964, R-82.

Cumby, T.R., 1987. A review of slurry aeration 3. Performance of aerators. J. Agric. Eng. Res., 36: 175-206.

Davis. Interfacial shear measurement for two-phase gas-liquid flow by means of Preston tubes. Ind. Eng. Chem. Fundam.1969, 8:153-159.

DeMoyer, C.D., E.L. Schierholz, J.S. Gulliver and S.C. Wilhelms, 2003. Impact of bubble and free surface oxygen transfer on diffused aeration systems. Water Res., 37: 1890-1904.

Descamps, M. N., Oliemans, R. V., Ooms, G., & Mudde, R. F. (2008). Air–water flow in a vertical pipe: Experimental study of air bubbles in the vicinity of the wall. Exp Fluids Experiments in Fluids, 45(2), 357-370. doi:10.1007/s00348-008-0484-6

Dinh, B.T. and T.S. Choi, 1999. Application of image processing techniques to air/water two-phase flow. Mech. Res. Commun., 26: 463-468.

Durst, F., Kikura, H., Lekakis, I., Jovanović, J., & Ye, Q. (1996). Wall shear stress determination from near-wall mean velocity data in turbulent pipe and channel flows. Experiments in Fluids, 20(6), 417-428. doi:10.1007/bf00189380

Ekambara, K., Sanders, R. S., Nandakumar, K., & Masliyah, J. H. (2012). CFD Modeling of Gas-Liquid Bubbly Flow in Horizontal Pipes: Influence of Bubble Coalescence and Breakup. International Journal of Chemical Engineering, 2012, 1-20. doi:10.1155/2012/620463

Fabre, L. Masbernat, and C.Suzanne. Stratified flow Part I: local structure, Multiphase Science and Technology. 1987, 3: 285-301.

Fayolle, Y., A. Cockx, S. Gillot, M. Roustan and A. Heduit, 2007. Oxygen transfer prediction in aeration tanks using CFD. Chem. Eng. Sci., 62: 7163-7171.

Govier, G.W., Aziz, K., 1972. The Flow of Complex Mixtures in Pipes. Van Nostrant-Reinhold Co., New York.

Hibiki, T., Ishii, M., 2002. Development of one-group interfacial area transport equation in bubbly flow systems. Int. J. Heat Mass Transfer 45, 2351–2372.

Ishii, M., & Kim, S. (2004). Development of One-Group and Two-Group Interfacial Area Transport Equation. Nuclear Science and Engineering Nucl. Sci. Eng., 146(3), 257-273. doi:10.13182/nse01-69

Iskandrani, A., Kojasoy, G., 2001. Local void fraction and velocity field description in horizontal bubbly flow. Nucl. Eng. Des. 204, 117–128.

Jakobsen, H. A. (2014). Chemical reactor modeling: Multiphase reactive flows. Cham: Springer.

Kim, T., Kim, Y., & Han, M. (2012). Development of novel oil washing process using bubble potential energy. Marine Pollution Bulletin, 64(11), 2325-2332. doi:10.1016/j.marpolbul.2012.08.031

Kirillov, I. P.Smogalev, M. Y Suvorov, R. V.Shumsky and Y.Stern. Investigation of steam-water flow characteristics at high pressures. Proc. 6th Int. Heat Transfer Conf., Toronto. 1978, pp. 315-320.

Kocamustafaogullari, G., & Wang, Z. (1991). An experimental study on local interfacial parameters in a horizontal bubbly two-phase flow. International Journal of Multiphase Flow, 17(5), 553-572. doi:10.1016/0301-9322(91)90024-w

Kocamustafaogullari, G., Huang, W.D., 1994. Internal structure and interfacial velocity development for bubbly 2-phase flow. Nucl. Eng. Des. 151, 79–101.

Kocamustafaogullari, G., Huang, W.D., Razi, J., 1994. Measurement and modeling of average void fraction, bubble size and interfacial area. Nucl. Eng. Des. 148, 437–453

Kowalski. Wall and interfacial shear stress in stratified flow in a horizontal pipe, AIChE J. 1987, 33: 274.

Lee, Taeyoon, Van Thinh Nguyen, "2D Numerical Simulations of Bubble Flow in Straight Pipes." 한국수자원학회 학술대회, (2016.05): P3-27.

Lehr, F., Millies, M., Mewes, D., 2002. Bubble-size distributions andflow fields in bubble columns. AIChE J. 48, 2426–2443.

Li, C., Cheung, S.C.P., Yeoh, G.H., Tu, J.Y., 2010. Modelling horizontal gas–liquid flow using averaged bubble number density approach. J. Comp. Multiphase Flows 2, 89–100.

Lo, S., Zhang, D.S., 2009. Modeling break-up and coalescence in bubbly two-phase flows. J. Comp. Multiphase Flows 1,23–38.

Martinez-Bazan, C., Montanes, J.L., Lasheras, J.C., 1999a. On the breakup of an air bubble injected into a fully developed turbulent flow. Part 1. Breakup frequency. J. Fluid Mech. 401, 157–182.

Martinez-Bazan, C., Montanes, J.L., Lasheras, J.C., 1999b. On the breakup of an air bubble injected into a fully developed turbulent flow. Part 2. Size PDF of the resulting daughter bubbles. J. Fluid Mech. 401, 183–207.

Prince, M. J., & Blanch, H. W. (1990). Bubble coalescence and break-up in air-sparged bubble columns. AIChE Journal AIChE J., 36(10), 1485-1499. doi:10.1002/aic.690361004

Razzaque, M.M., Afacan, A., Liu, S., Nandakumar, K., Masliyah, J.H., Sanders, R.S., 2003. Bubble size in coalescence dominant regime of turbulent air-water flow through horizontal pipes. Int. J. Multiphase Flow 29, 1451–1471.

Sanders, R.S., Razzaque, M.M., Schaan, J., Nandakumar, K., Masliyah, J.H., Afacan, A., Shijie, L., 2004. Bubble size distributions for dispersed air – water flows in a 100 mm horizontal pipeline. Can. J. Chem. Eng. 82, 858–864.

Taitel, Y., Dukler, A.E., 1976. Model for predicting flow regime transitions in horizontal and near horizontal gas–liquid flow.AIChE J. 22, 47–55.

Talley, J.D., Kim, S., 2010. Horizontal bubbly flow with elbow restrictions: interfacial area transport modeling. Nucl. Eng. Des. 240, 1111–1120.

Tselishcheva, E.A., Antal, S.P., Podowski, M., 2010. Mechanistic multidimensional analysis of horizontal two-phase flows. Nucl. Eng. Des. 240, 405–415.

Vershinin, V. E., Ganopolsky, R. M., & Polyakov, V. O. (2015). Numerical Modeling of Two-Dimensional Gas-Liquid Flow Structures. Modern Applied Science MAS, 9(2). doi:10.5539/mas.v9n2p236

Weisman, J., Duncan, D., Gibson, J., Crawford, T., 1979. Effects of fluid properties and pipe diameter on 2-phase flow patterns in horizontal lines. Int. J. Multiphase Flow 5, 437–462.

Whalley and K. W.McQuillan. The development and use of a directional wall shear stress probe. 2nd Int. Conf. on Multiphase Flow London, 1985, Paper G2.

Wu, Q., Kim, S., Ishii, M., Beus, S.G., 1998. One-group interfacial area transport in vertical bubbly flow. Int. J. Heat Mass Transfer 41, 1103–1112.

Yang, J., Zhang, M.Y., Su, Y., Zhang, C., 2004. Quasi 3-D measurements of turbulence structure in horizontal air-water bubbly flow. Nucl. Eng. Des. 227, 301–312.

Yao, W., Morel, C., 2004. Volumetric interfacial area prediction in upward bubbly two-phase flow. Int. J. Heat Mass Transfer 47, 307–328.

Yeoh, G., Cheung, S. C., & Tu, J. (2012). On the prediction of the phase distribution of bubbly flow in a horizontal pipe. Chemical Engineering Research and Design, 90(1), 40-51. doi:10.1016/j.cherd.2011.08.004

Yin, Z., Zhu, D. Z., Cheng, D., & Liang, B. (2013). Oxygen Transfer by Air Injection in Horizontal Pipe Flow. J. Environ. Eng. Journal of Environmental Engineering, 139(6), 908-912. doi:10.1061/(asce)ee.1943-7870.0000680

초록

Water Aeration 의 주요 목적은 물속의 용존산소 농도를 적정 수준으로 유지 함으로써 수질을 개선하는 것이다. 일반적으로 파이프를 통해 기포를 주입하는 방법으로 이뤄지며, 기포의 크기가 작을수록 DO 의 농도를 높이는 데에 효과적이다. Water Aeration 파이프 시스템 디자인에 있어 가장 크게 고려되는 점은 어떻게 하면 최대한 작은 기포를 생성할 수 있는가 이다. 본 연구의 목적은 직관 내에서 물-공기(two-phase flow) 혼합물의 흐름으로 인해 발생하는 벽 전단력이 기포 크기에 어떠한 영향을 미치는지 분석하는 것이다.

Kocamustafaogullari and Wang (1991), Yin et al. (2012), 상수도시스템실험실의 실험 자료를 바탕으로 수평의 직관 내에 흐르는 two-phase flow 에 대해 2 차원 수치해석을 시행하였다. 오일러-오일러 방식과 조합된 RANS 모델과 dispersed k-ε 모델을 사용하였고, 기포의 결합과 분리현상의 고려하에 Interfacial Area Transport Equation (IATE) 모델을 사용하여 기포 크기의 분포도를 해석하였다.

Kocamustafaogullari and Wang (1991)의 유속 분포도와 기포 크기 분포도 자료를 상대로 모델의 타당성을 검증하였고, 평균 오차 범위는 각각 4%~15%, 8%~30%이었다. 이후, 각 실험의 조건을 토대로 여러 직관 내 흐름에 대한 수치해석을 하여 벽 전단력을 계산하였다. 실험과 수치해석 결과 간의 상관관계를 분석하였으며, 분석 결과, 파이프의 벽 전단력이 높거나 물과 공기의 혼합물이 벽 전단력에 오랜 시간 영향을 받는다면, 기포의 크기가 작아진다는 것을 알 수 있었다.

주요어: 전산유체역학, OpenFOAM, 2 차원 수치모의, Two-Phase, 기포의 결합과 분리, Sauter Mean Diameter, 용존산소
학번: 2014-22711